Validation of a Flexible Bilayer Micro-Electrocorticography Array and Extraction of High-Frequency Features of Neuronal Activity

by

Cody Barton

A Dissertation Presented in Partial Fulfillment
of the Requirements for the Degree
Doctor of Philosophy

Approved November 2018 by the
Graduate Supervisory Committee

Bradley Greger, Chair
Marco Santello
Chistopher Buneo
Oliver Graudejus
Panagiotis Artemiadis

ARIZONA STATE UNIVERSITY

December 2018

ABSTRACT

Neural interfacing applications have advanced in complexity, with needs for increasingly high degrees of freedom in prosthetic device control, sharper discrimination in sensory percepts in bidirectional interfaces, and more precise localization of functional connectivity in the brain. As such, there is a growing need for reliable neurophysiological recordings at a fine spatial scale matching that of cortical columnar processing. Penetrating microelectrodes provide localization sufficient to isolate action potential (AP) waveforms, but often suffer from recorded signal deterioration linked to foreign body response. Micro-Electrocorticography (μECoG) surface electrodes elicit lower foreign body response and show greater chronic stability of recorded signals, though they typically lack the signal localization necessary to isolate individual APs. This dissertation validates the recording capacity of a novel, flexible, large area μECoG array with bilayer routing in a feline implant, and explores the ability of conventional μECoG arrays to detect features of neuronal activity in a very high frequency band associated with AP waveforms.

Recordings from both layers of the flexible μECoG array showed frequency features typical of cortical local field potentials (LFP) and were shown to be stable in amplitude over time. Recordings from both layers also showed consistent, frequency-dependent modulation after induction of general anesthesia, with large increases in beta and gamma band and decreases in theta band observed over three experiments. Recordings from conventional μECoG arrays over human cortex showed robust modulation in a high frequency (250-2000 Hz) band upon production of spoken words. Modulation in this band was used to predict spoken words with over 90% accuracy. Basal Ganglia neuronal AP

firing was also shown to significantly correlate with various cortical µECoG recordings in this frequency band. Results indicate that µECoG surface electrodes may detect high frequency neuronal activity potentially associated with AP firing, a source of information previously unutilized by these devices.

TABLE OF CONTENTS

Page

LIST OF TABLES

Table Page

LIST OF FIGURES

Figure Page

Figure Page

Chapter 1

INTRODUCTION

Electrocorticography grids are designed to record neuronal activity from the cerebral cortex, whose basic functional unit is the cortical column, a grouping of neurons with similar receptive fields and processing preferences with a diameter on the order of hundreds of microns (Mountcastle, 1997). The spatial extent of the local field potential (LFP) signals recorded from micro-electrocorticography (μECoG) arrays falls in a similar range; size estimates of the region of neural tissue contributing to the LFP signal range from hundreds of microns to a millimeter or more (Katzner, 2009; Xing, 2009; Leski, 2013). Micro-scale Electrocorticography electrodes, with diameters on the order of 100 μm or sometimes less, allow for examination of these LFP signals at a submillimeter scale, finer than what is possible using larger, clinical ECoG electrodes with diameters of several mm (Kellis, 2016). This finer scale allows for examination of lower-level computational processes in the cortex and may improve the signal specificity needed for neuroprosthetics applications that involve multiple degrees of freedom, such as volitional control of individual finger movements or real-time decoding of speech from neural signals.

Although intracortical penetrating microelectrodes record neural signals at the finest spatial scale and specificity, their usage inevitably causes some degree of tissue damage as the cortical surface is pierced. The tissue response to these devices may include disruption of vasculature, a chronic inflammatory response leading to glial scarring around the device surface, and neuronal degeneration in the implant area (Biran et al 2005, McConnell et al 2009). This tends to cause reduction in signal quality over time, both in

the number of neurons recorded and their signal amplitude (Schwartz et al 2006, Chestek et al 2011, Jorfi, 2015). Substantial loss of signal quality from intracortical multielectrode arrays often happens within a timeframe of 6-12 months (Ryu, 2009). Additionally, fibrous encapsulation and meningeal tissue proliferation may on occasion dislodge the implanted microelectrode device (Barrese 2013).

Cortical surface arrays, by contrast, are often assumed not to elicit a substantial biological reaction as their usage does not penetrate the cortex, avoiding disruption of the blood-brain barrier and lessening the mechanical strain inherent to the interaction between rigid electrodes implanted in soft cortical tissue. However, while few studies have assessed long-term host-tissue response to epidural or subdural grids, some foreign body response has nevertheless been observed. Post-mortem histological examination of rat brains subdurally implanted with µECoG arrays has revealed mild, chronically granulated inflammation in the leptomeninges around the implant area (Henle 2011). Studies examining tissue growth around epidural ECoG arrays using cranial window imaging found substantial vascular changes as well as dural thickening under the arrays and tissue encapsulation over the top of the array (Schendel 2013; Schendel 2014). A study of ECoG electrodes implanted in a Rhesus Macaque for 22 months found macrophages and foreign body giant cells at the tissue-array interface and collagenous tissue encapsulation of the grid (Degenhart 2016). However, in spite of the stereotypical foreign body response, this study found that damage to the cortex underneath the implant was minimal, microglia were not actively responding to trauma, and importantly, recordings 18 months post implant still showed robust signal modulation during a hand movement task. Additionally, despite the

encapsulation, the array was removed from the fibrous tissue with little resistance, indicating minimal adhesion between encapsulation tissue and the device.

In addition to the reduced tissue response of surface electrodes compared to penetrating electrodes, Local Field Potentials, which can be recorded from surface electrodes or penetrating electrodes, can show greater long-term stability than the action potential waveforms recorded from penetrating electrodes. A decoder of arm motion from surface electrodes in monkeys showed stability over months without drift in accuracy or recalibration (Chao, 2010). Depending on the frequency band, LFP signals recorded from penetrating microelectrodes may show insignificant reduction in mean power over time, or reduction at a rate much slower than the concurrent decrease in spike count and signal-to-noise ratio of isolated action potential waveforms and multiunit activity from the same electrodes (Wang 2014; Perge 2014; Zhang 2018). Movement-related information in LFP signals can remain high even when spikes can no longer be detected from the same electrode (Flint, 2012). Overall, µECoG surface electrode arrays represent a balance between the localization of specific neural signals with a level of invasiveness and longevity suitable for chronic applications in brain-computer interfaces or the study and monitoring of neurological disorders in human subjects.

While µECoG arrays have conventionally been used only to record and analyze low-frequency neural signals below approximately 200 Hz, features of neuronal spiking are thought to "bleed" into the upper frequencies of conventional LFP bands (Manning, 2009; Ray, 2011). Given that volume conduction in neural tissue may have primarily resistive rather than frequency-dependent properties (Logothetis, 2007), it is possible that even higher frequency bands may contain more direct features of spiking activity when

recorded by surface μECoG electrodes. Action potentials arguably form the main form of communication in the nervous system (Khodagholy, 2015), and their detection from surface μECoG arrays would effectively provide these arrays with some of the localization and specificity advantages of intracortical arrays without requiring as much invasiveness.

The specificity and localization of recordings from surface electrodes may also be improved through the design of thin and conformable arrays that can better match the curved geometry of the cortical surface. Flexible arrays that more closely match the mechanical impedance of neural tissue could also potentially reduce tissue irritation (Lacour, 2010), possibly improving device performance and longevity. Micro-Electrocorticography grids tailored to the mechanical and electrophysiological properties of neural tissue at fine spatial scales could potentially allow for greater detection of aspects of neuronal spiking activity, expanding the categories of information available for control signals in neuroprosthetics applications that use surface electrodes. Applications for clinical monitoring or study of neurological disorders could similarly benefit from access to potential features of action potential spiking activity as recorded from surface electrodes, possibly containing biomarkers of cortical pathology, without needing to penetrate the cortical surface.

Chapter 2

VALIDATION OF A MECHANICALLY COMPLIANT, LARGE AREA, HIGH RESOLUTION MICRO-ELECTROCORTICOGRAPHY ARRAY WITH BILAYER ROUTING

ABSTRACT

Thin, mechanically compliant micro-Electrocorticography (μECoG) arrays have the potential to improve the quality and reliability of brain-computer interfaces in a variety of applications. Compared to commercially available macro or micro-scale Electrocorticography grids, micro-scale flexible surface electrode arrays may potentially achieve improved proximity to the curved cortical tissue surface. Access to cortical sulci, which compose up to 2/3 of the human cortex, may be achieved more easily with mechanically compliant arrays. Greater proximity to the cortical surface may improve signal specificity and integrity (Kellis, 2011), while reduced mechanical impedance mismatch between a flexible substrate and the small elastic modulus of neural tissue may result in lessened tissue response, potentially improving device longevity and reliability. While μECoG electrodes offer a sub-millimeter spatial recording scale (Kellis, 2011) comparable to the reach of local field potentials and suitable for interfacing with cortical columnar structures, applications such as epileptic foci localization require broad cortical coverage. Many μECoG arrays are insufficient for these applications, covering only tens of mm^2, albeit at a fine spatial resolution.

To address these needs, the prototype μECoG electrode array used in this study employs a novel bilayer construction, routing gold wire traces over two stacked levels with the goal of increasing electrode density and number on a flexible Polydimethylsiloxane (PDMS) substrate. To validate the recording and stimulation characteristics of the bilayer

routing design, three iterations of arrays were implanted in feline models, targeting the motor cortex for regular recording sessions and stimulation experiments. Neural signals recorded from both layers of the device showed elevated mid-frequency structure typical of local field potential (LFP) signals that was stable in amplitude over implant duration, and also exhibited consistent frequency-dependent modulation after anesthesia induction by Telazol in three separate experiments. Cortical stimulation through the device, however, was not successful in evoking muscle twitches, possibly due to very high impedance or open circuits in the early device iterations coupled with a potential lack of viable electrodes over the relevant areas of cortex. Overall, the bilayer routing technique shows promise as a method to increase density of electrode routing on flexible substrates, and the issues with impedance and connectivity discovered in this study could be possibly improved upon with alternate methods of connecting the wire traces to a head stage

INTRODUCTION

Electrophysiological recordings in both clinical and neuroprosthetics research applications must compromise between signal localization at fine spatial scales and the invasiveness required to obtain more local signals. The basic functional unit of the cortex is the cortical column (Mountcastle 1997), which is formed of a grouping of neurons with similar receptive fields and processing preferences. The size of cortical columns is on the order of hundreds of microns. Similarly, the spatial extent of the local field potential (LFP) signals recorded from µECoG arrays ranges from hundreds of microns to a millimeter or more (Leski, 2013). Micro-scale Electrocorticography (µECoG) electrode arrays, with electrode diameters around 100 µm, allow for examination of these LFP signals at a millimeter to submillimeter scale, finer than what is possible using larger, clinical macro-

scale ECoG electrodes with diameters of several mm that record the summed activity of correspondingly larger volumes of neural tissue (Kellis, 2016). Although intracortical penetrating microelectrodes record neural signals at the finest spatial scale and specificity, they typically cause some degree of tissue damage, foreign body response and degradation of neural signal over time (Jorfi, 2015); substantial loss of signal quality from intracortical multielectrode arrays often happens within a timeframe of 6-12 months (Ryu, 2009). Epicortical electrode arrays do not puncture the cortical surface and thus represent a balance between the localization of specific neural signals with a level of invasiveness and longevity suitable for chronic applications in brain-computer interfaces or the study and monitoring of neurological disorders.

There is a need for thin and mechanically compliant μECoG arrays in both clinical and neuroprosthetics research applications. The human cortex is highly gyrencephalic, with around two thirds of its surface buried in sulci and only one third exposed in the gyri (Ribas, 2010). Focal cortical dysplasia lesions causing epilepsy can develop within fissures and sulci, increasing the difficulty of diagnosis (Besson, 2008). Large portions of the auditory cortex in humans and macaques are in the lateral sulcus (Hackett, 2011), and areas of V1 cortex corresponding to peripheral and parafoveal vision lie within the calcarine and saggital fissures (Christie, 2016). These sulci are inaccessible to conventional clinical subdural ECoG arrays (Khodagholy, 2015), but thin, flexible μECoG arrays have recently been used to record LFP signals from cerebral sulci in macaque monkeys (Matsuo, 2011; Fukushima, 2014).

Currently available µECoG grids are often stiff and do not conform well to the curvilinear cortical surface, which can decrease device stability and efficacy. Lack of array conformance may also introduce cerebrospinal fluid between the device and the cortex, giving a degree of electrical continuity between electrodes and effectively reducing signal localization and spatiotemporal detail (Kellis, 2011). Flexible µECoG array designs could thereby potentially improve electrode conformance and proximity to the cortical surface, and thereby improve the specificity and integrity of the recorded neural signals. Recently, highly localized action potential waveforms were recorded from a thin, flexible, micro-scale array with 10 µm diameter electrodes. (Khodagholy, 2015). Additionally, thin and flexible designs may reduce tissue irritations by lowering the mechanical impedance of the device closer to the small elastic modulus of cells and biological tissue (Lacour, 2010).

While many applications of neural interfaces benefit from the high signal integrity and specificity offered by micro-scale electrodes, some applications require coverage of large areas of cortex (80mm x 80mm), such as localization of epileptogenic zones. Brain-computer interfaces requiring specific, localized signals may also benefit from µECoG arrays with high spatial resolution over large areas, as the location of functional areas of the cortex may vary by at least 5mm across subjects (Viventi, 2011), and commercially available µECoG grids are often only 4mm on a side. The µECoG array in this study is designed to address both needs with a scalable design of 96 micro-scale (100-300 µm) recording sites on a flexible polydimethylsiloxane (PDMS) grid with a 2mm electrode pitch. The total number and density of electrodes may scale upwards by separating the routing of thin gold film wire traces in a bi-level metallization process. The primary

purpose of this study was to validate the recording and stimulation capabilities of the bilayer device design in chronic feline implantations.

METHODS

Array design and fabrication. A 96-channel microelectrode array was made by patterning a thin gold film onto a polydimethylsiloxane (PDMS) substrate with a thermal evaporator. Bi-level metallization split the wire routing onto two PDMS layers to increase electrode density. Electrode contact sites were formed with 100-300 µm diameters and 2mm spacing on a 20mm x 20mm PDMS grid. The gold film traces connect to contact points on a printed circuit board using silver paste to mediate electrical contact, and the assembly was physically secured by compression bonding with a second PCB. The assembly connects to an acquisition system via a Tucker-Davis Technologies Zero Insertion Force connector. A pedestal was 3D printed with a titanium base (Protolabs, Maple Plain, MN) and a lightweight plastic lid and wall to house the PCB and secure it to the skull, and the assembly was potted with medical epoxy to prevent ingress of fluid.

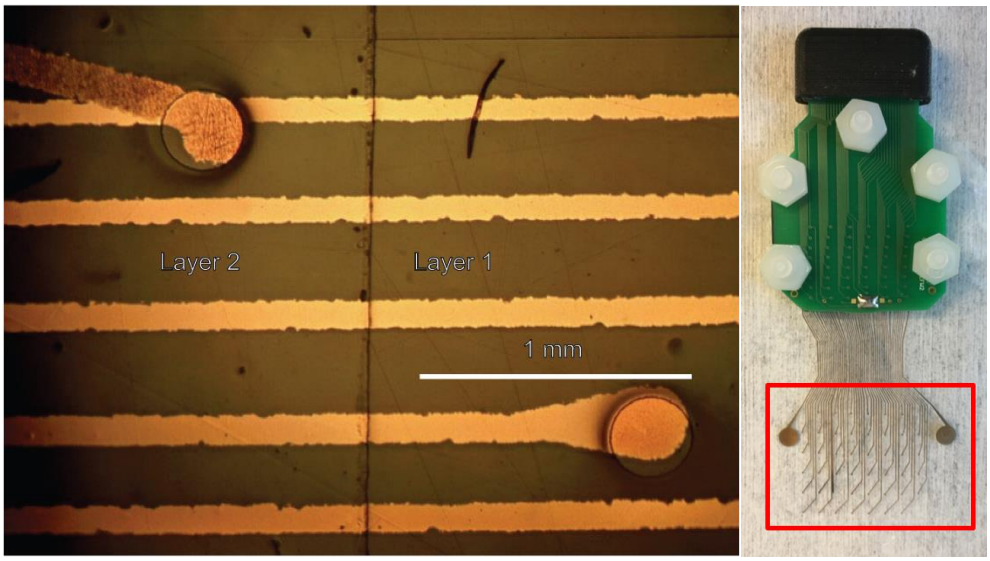

Figure 2.1. Bilayer Organization and Assembled Array. Gold wire traces were patterned onto stacked PDMS substrate layers. Exposed electrode contacts are 200 µm in diameter and spaced 2mm apart. Layer 2, situated on top of Layer 1, contains the proximal half of the electrodes relative the PCB attachment Its PDMS substrate terminates halfway down the grid, shown in the center of the left image, leaving Layer 1 uncovered in the distal half of the grid.

Surgical Implant. For each feline implant, a craniotomy was performed between the lambdoidal and frontal sutures, extending approximately 15-20 mm anterior – posteriorly and 18mm laterally from the edge of the sagittal suture. The craniotomy exposed the majority of one cortical hemisphere The electrode grid was trimmed intraoperatively when necessary to fit the size of the craniotomy, which varied between animals based on the constraints of suture location. The electrode array was placed on the cortical surface with electrodes in the most medial and anterior corner targeting sensorimotor cortical areas (Figure 2.2) and the bone flap was reattached with a titanium strip after securing the pedestal to the skull (Figure 2.3).

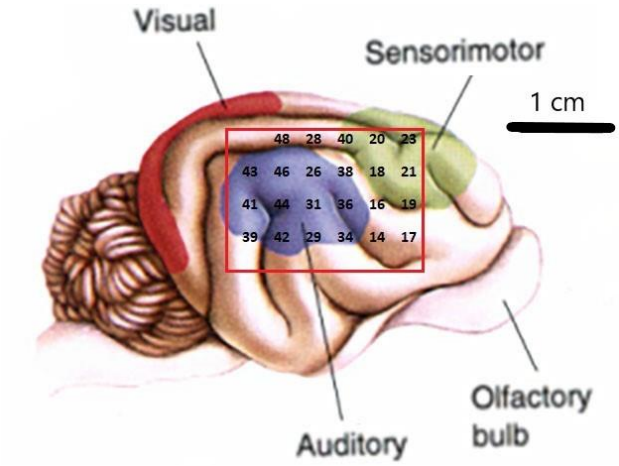

Figure 2.2. Schematic of Implant Location**.** The red outline indicates the approximate size and implant location of the 1st implant, which had only 48 electrodes, of which all but 23 were trimmed off due to minimal area between sutures and the resulting small allowable craniotomy size in the first feline.

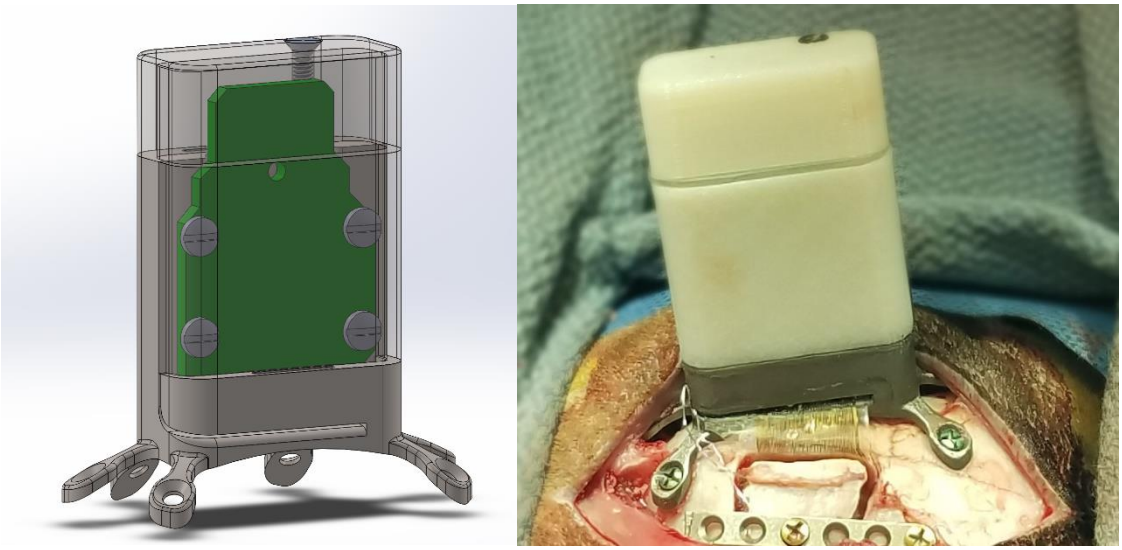

Figure 2.3. Pedestal Schematic and Surgical Implant. The pedestal body was 3D printed from titanium, while the lid and wall components were 3D printed from lightweight plastic to reduce the weight carried by the animal. The image on the right shows implant

placement during surgery, with the craniotomy for the electrode grid positioned just lateral of the sagittal suture and just caudal of the frontal suture in order to target motor cortical areas.

Stimulation. To evoke muscle twitches, epicortical stimulation pulses were delivered through individual electrodes of the bilayer array. Biphasic, charge-balanced stimulus trains of 0.6 ms phase duration and 0.3ms phase delay were delivered with a pulse frequency of 300 Hz in stimulus trains lasting 400 ms. Stimulus amplitude began at 1 μA and increased in 50 μA increments until a maximum of 300 μA was reached. EMG recordings were simultaneously taken from the contralateral hind limb of the anesthetized animal to confirm the presence of muscle twitches upon stimulus delivery.

Analysis. Electrophysiological recordings during the awake state began after the animal had recovered from surgical implant, and were taken at a sampling rate of 10 kHz. Multi-taper spectral estimates with a time-bandwidth product of 5 were used to compute frequency spectrums of recorded signals, and mean spectrum intensity was calculated in five LFP frequency bands: Theta band (θ, 3-8 Hz); Alpha band (α, 7-16 Hz); Beta band (β, 15-32 Hz); Gamma band (γ, 31–80 Hz); and Chi band (χ, 79-161 Hz). Impedance measurements were taken using a TDT PZ5 NeuroDigitizer probing at 1120Hz.

To validate the neural origin of the recorded signals, recordings were taken during the emergent recovery period approximately 1 hour after induction of general anesthesia via 10 mg/kg Telazol injection to compare against the awake state. For comparisons of spectrums from electrodes on different array layers and for comparisons between awake and anesthetized states, spectrum distributions were sampled by segmenting 1-minute

portions of continuous recordings into 12 nonoverlapping 5-s windows, and spectrums were computed for each window. Comparisons between awake and anesthetized states on the same electrodes were tested for significant change in each frequency band using a nonparametric, paired difference Wilcoxon signed-rank test. Comparisons between electrodes from different layers were tested for significant difference in distribution using a nonparametric Wilcoxon rank-sum test. Significance was defined at $\alpha = .05$, and Bonferroni correction was applied for the number of tests per frequency band. For each layer, viable electrodes were defined as those that registered an impedance value on the PZ5 NeuroDigitizer on any session. Electrodes that failed to register an impedance value below the device cutoff of 536 kOhm were excluded from analysis.

Chronic stability of recorded neural signals from viable electrodes was assessed for each frequency band in both layers via linear regression on the median spectrum amplitude over time. A Linear Hypothesis Test was performed on each regression result to determine trends significantly different from flat slope.

RESULTS

Troubleshooting. The recordings taken from the first feline implanted showed large groups of adjacent channels with identical or strongly correlated recordings, indicating electrical continuity between electrodes. Disassembly of another 1st iteration prototype grid revealed spreading of the silver paste caused by the compression bonding technique (Figure 2.4). To reduce the shorting between adjacent wire contact sites, laser-cut masks were used in future device iterations along with reduced electrode density. Impedance testing on the first device showed all impedances greater than the TDT 536

kOhm cutoff, and attempts to evoke muscle twitches through cortical stimulation in the anesthetized feline were unsuccessful. However, stimulus artifacts from the cortical array were detected from an EMG recording setup with fine-wire electrodes placed in the animal's hind limb.

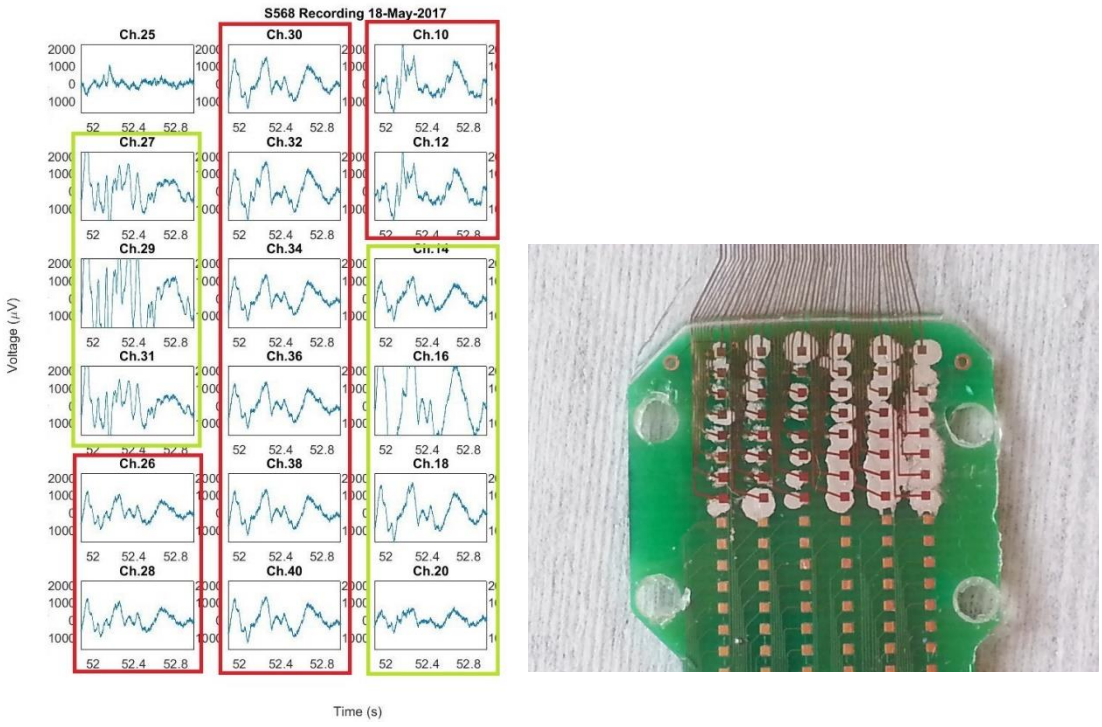

Figure 2.4. Electrical Shorting Between Channels**.** Left, signals recorded from the implanted first iteration array showed a substantial number of channels with nearly identical or similar recordings, indicating some electrical continuity between channels. Right, disassembly of a 1st generation array revealed spreading of the silver paste, caused by the compression bonding technique.

The 2nd generation array with more precise silver paste application had fewer electrically shorted channels, but was also unsuccessful at evoking muscle twitches by

cortical stimulation, despite having successfully recorded sinusoidal signals from a function generator through a saline medium during *in vitro* pre-implant testing. Further testing of the explanted array revealed very low amplitude of a test sinusoidal electrical signal passed through each electrode separately and recorded by a probe with input impedance in the mega-Ohm range, consistent with impedances also in the mega-Ohm range for electrode contact sites (Figure 2.5). Electroplating of electrodes on the assembled device was performed in the 3rd iteration array to reduce electrode contact impedance.

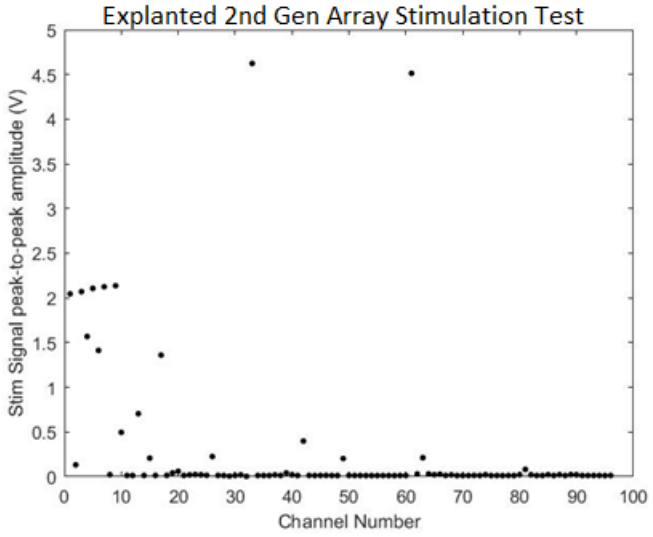

Figure 2.5. 2nd Iteration Array Stimulation Testing. A 1 kHz sinusoidal signal from a function generator was passed through the electrode array in a saline medium and recorded by a probe with input impedance in the MOhm range. No electrodes except the large reference pads were able pass a signal through the saline at a probe voltage greater than 50% of the source signal, with all but nine electrodes at less than 10%, indicating impedances in the MOhm range or open circuit for electrode contact sites.

After electroplating of the 3rd generation array, stimulation testing for the 3rd iteration electrode array showed 36 of 65 electrodes that could pass the *in vitro* saline

stimulation test at or near input voltage (Figure 2.6), consistent with electrode impedances in the tens to low hundreds of kOhms. These electrodes with low impedance included nine in a corner of the array suitable for placement over motor cortex (ch. 45, 31, 38, 37, 48, 34, 47, 26, 40; Figure 2.7), although these electrodes and many others showed drastically lowered stimulation testing amplitudes after pedestal mount (Figure 2.7; Figure 2.8). However, while most changes were reductions in amplitude, eight channels actually increased in amplitude after mounting to the pedestal. It was then discovered that solder contact pads for newly added backup reference wires were bending the PCB, preventing flush attachment to the pedestal (Figure 2.9). The array assembly was removed from the pedestal, the solder contact pads and attached backup reference wires were removed from the PCB, and the array was again tested for stimulation capacity of its electrodes. After confirmation that stimulation capacity had been restored to many of the affected electrodes, including all in the corner targeting motor cortex except channels 31 and 47 (Figure 2.10, left), the assembly was again mounted to the pedestal. The second pedestal mounting resulted in some channels again losing stimulation capacity, while several others actually improved stimulation capacity relative to the second unmounted state, e.g. channel 31 (Figure 2.10; Figure 2.11). As several electrodes in the corner of the array targeting motor cortex were still able to pass a stimulation signal at high amplitude, this configuration was implanted in the third feline.

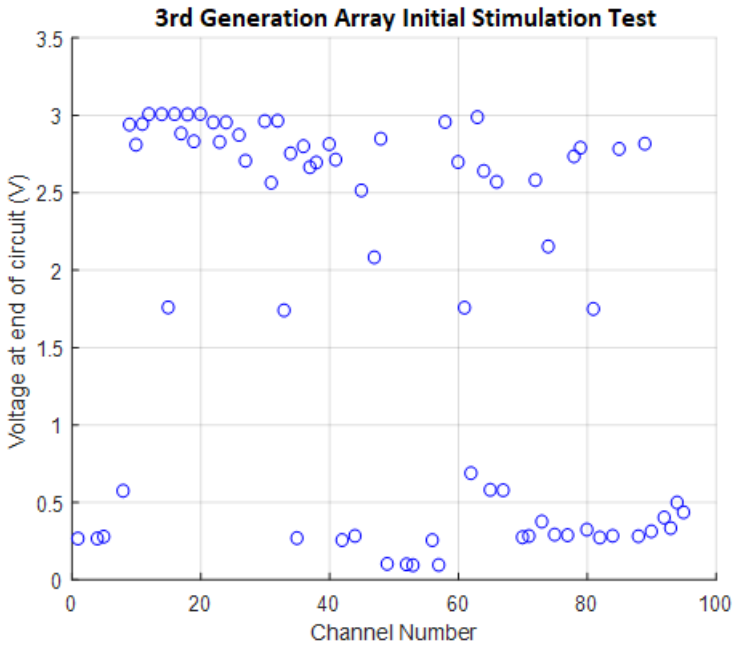

Figure 2.6. Stimulation testing for 3rd Generation Array. A 1kHz signal from a function generator was passed through the electrode array in a saline medium. 36 of 65 electrodes passed the 3V signal to a high input impedance probe through a saline medium at 2.5 V or higher, consistent with electrode impedances in the tens to low hundreds of kOhms.

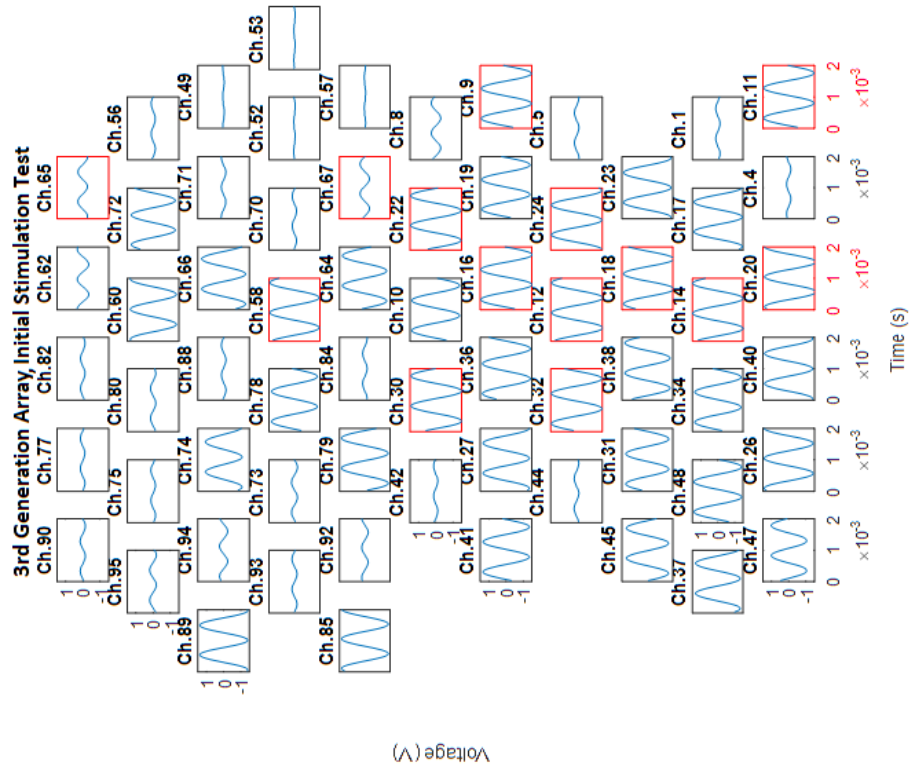
3rd Generation Array, Initial Stimulation Test
Voltage (V)
Time (s)

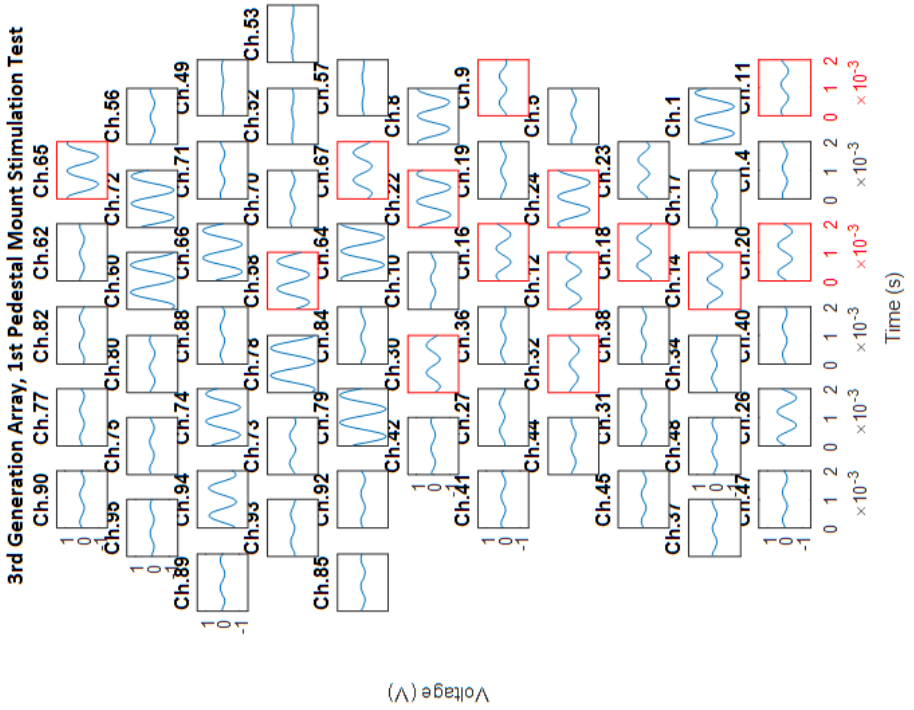
3rd Generation Array, 1st Pedestal Mount Stimulation Test
Voltage (V)
Time (s)

Figure 2.7. Stimulation Testing for 3rd Generation Array, 1st Pedestal Mount. Left, the recorded output of the stimulation test for the 3rd iteration array is shown before pedestal mount. Right, stimulation output amplitude was reduced for many electrodes after pedestal mount, including those in the lower left corner targeting motor cortex upon implant (Channels 45, 31, 38, 37, 48, 34, 47, 26, 40). Red outlined subplots indicate electrodes that exhibited electrical continuity with other electrodes.

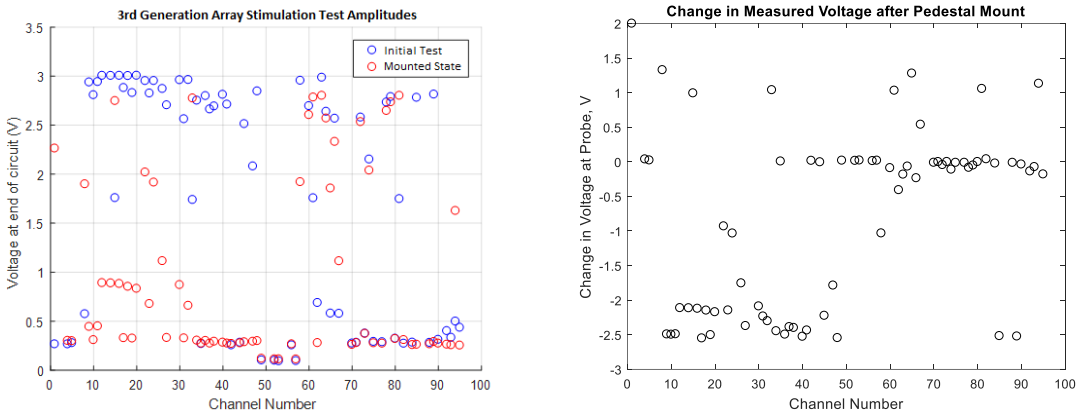

Figure 2.8. Change in Stimulation Amplitude After First Pedestal Mount**.** Left, the stimulation output amplitudes are shown for the 3rd generation array prior to mounting to the pedestal (blue) and after mounting to the pedestal (red). Right, the difference in stim amplitude output after mounting to the pedestal a second time is shown for each electrode. While most changes are reductions in amplitude, eight channels actually showed increases after the PCB was mounted to the pedestal in a bent configuration (Figure 2.9).

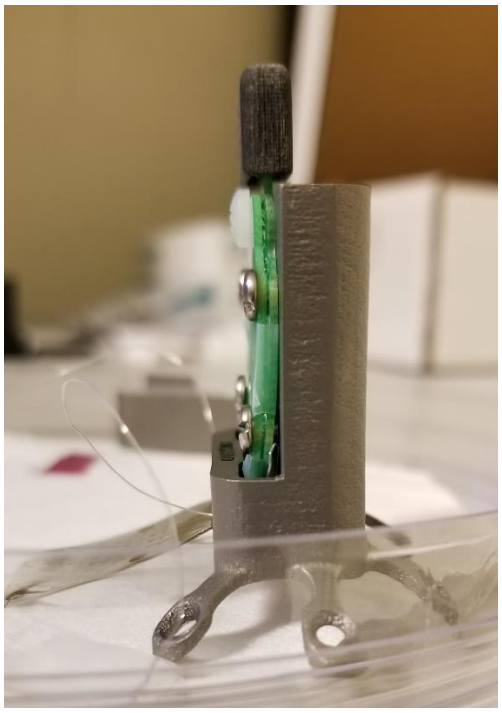

Figure 2.9. Strained PCB after Pedestal Mount. The first pedestal mount of the 3rd generation device resulted in reduced stimulation test amplitude on many channels. It was discovered that solder pads for backup reference wires were preventing the PCB assembly from making flush alignment with the pedestal and bending the bottom of the array, necessitating the removal of the PCB assembly, removal of the solder pads and backup reference wires, and remounting of the PCB assembly.

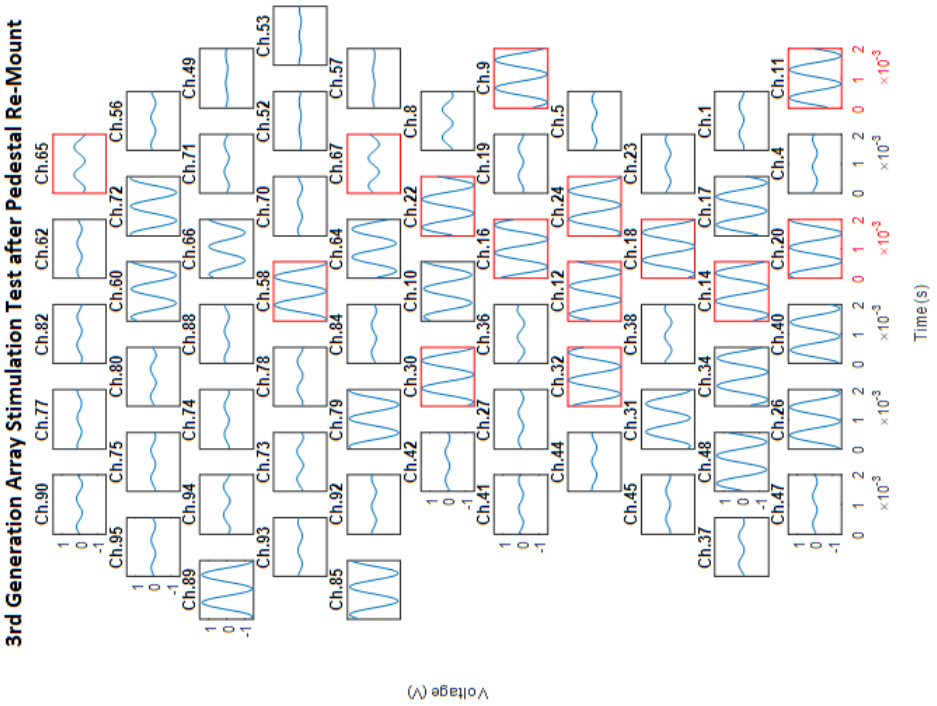
3rd Generation Array Stimulation Test after Pedestal Re-Mount
Voltage (V)
Time (s)

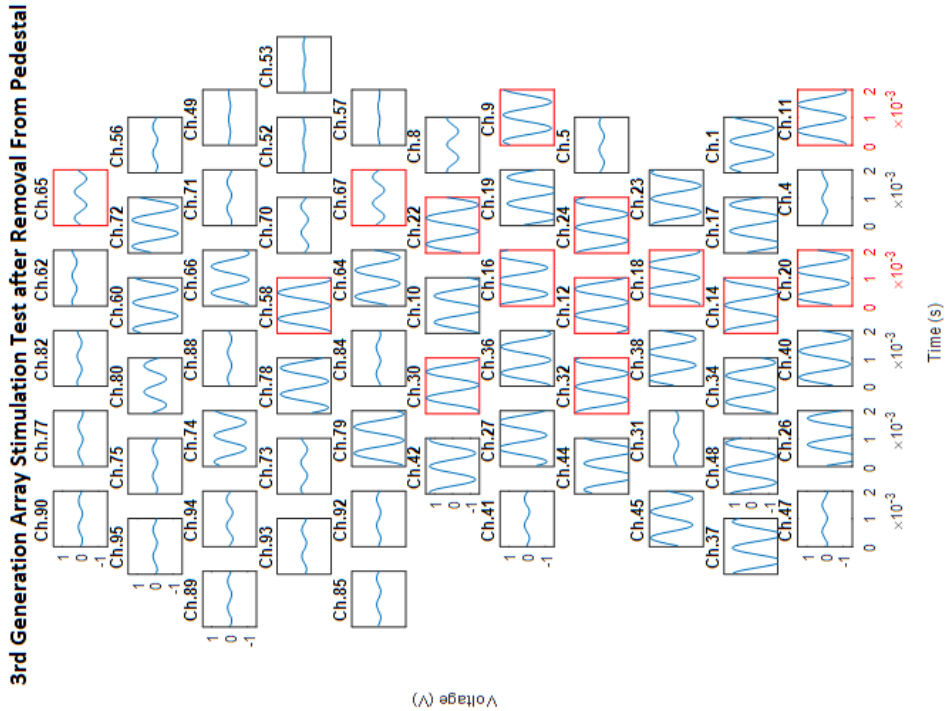
3rd Generation Array Stimulation Test after Removal From Pedestal
Voltage (V)
Time (s)

Figure 2.10. Stimulation Testing for 3rd Generation Array, Second Pedestal Mount**.** Left, the recorded output of the stimulation test for the 3rd iteration array is shown after removal from the first pedestal mount and prior to mounting for the second time. After removal, many channels regained stimulation capacity that had been lost after the first pedestal implant (Figure 2.7), notably channels 45, 37, 48, 34, 26, and 40 in the lower-left corner targeting motor cortex. Right, stimulation output amplitude after remounting the assembly to the pedestal shows reduction in some channels. Five channels in the lower left corner targeting motor cortex (ch. 31, 48, 34, 26, 40) were still able to pass high amplitude stimulation signal after the second pedestal mounting. Of these, channel 31 actually regained stimulation capacity compared to the prior unmounted state, showing more than 2V of increase in peak-to-trough amplitude after remounting to the pedestal.

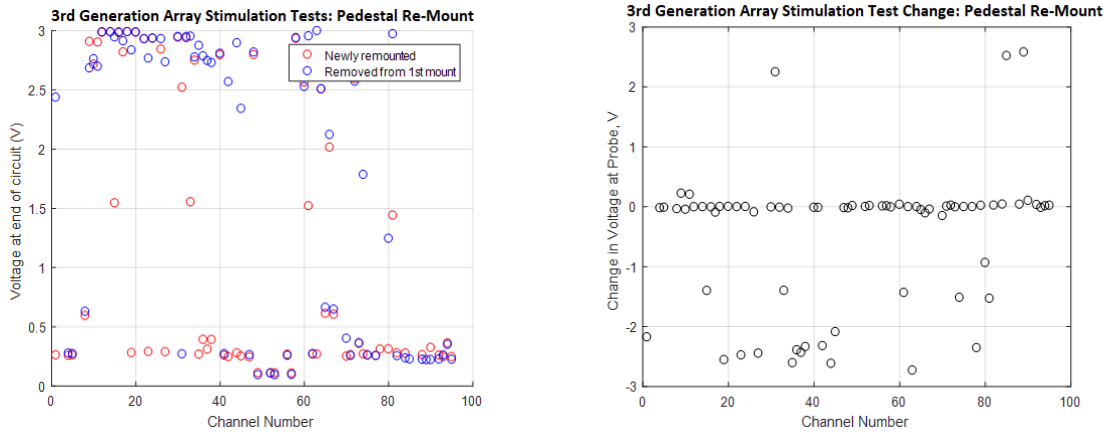

Figure 2.11. Change in Stimulation Amplitude After Second Pedestal Mount. Left, the stimulation output amplitudes are shown for the 3rd generation array after removal from the 1st pedestal mount (blue) and after mounting to the pedestal a second time (red). Right, the difference in stim amplitude output after mounting to the pedestal a second time is shown

for each electrode. While most changes were reductions in amplitude, three channels actually showed increases.

For the 3rd generation implanted array, 27 of 65 electrodes registered valid impedance measurements below the TDT PZ5 cutoff of 536 kOhm on at least one recording session. The 27 electrodes included 10 of 32 electrodes in Layer 1, and 17 of 33 electrodes in Layer 2 (Figure 2.12). A connection issue manifested 28 days post implant, causing most measurements to fail to register beneath the device maximum, although no interruption in recorded signals was observed at this time. Prior to 28 days post implant, of the five channels in the most medial and anterior corner targeting motor cortex, channels 31, 48, and 34 registered mean impedances of 63.3 kOhm, 96.3 kOhm, and 64 kOhm, respectively. The remaining two channels, 26 and 40, did not register impedances beneath 536 kOhm, despite previously successful stimulation testing after the final pedestal mount. Prior to 28 days post implant, viable electrodes on layer1 had a median impedance of 50.2 kOhm (37.4 – 61.9 kOhm for 25th and 75th percentiles), while viable electrodes on layer 2 had a median impedance of 31.7 kOhm (23.1 – 56.1 kOhm for 25th and 75th percentiles).

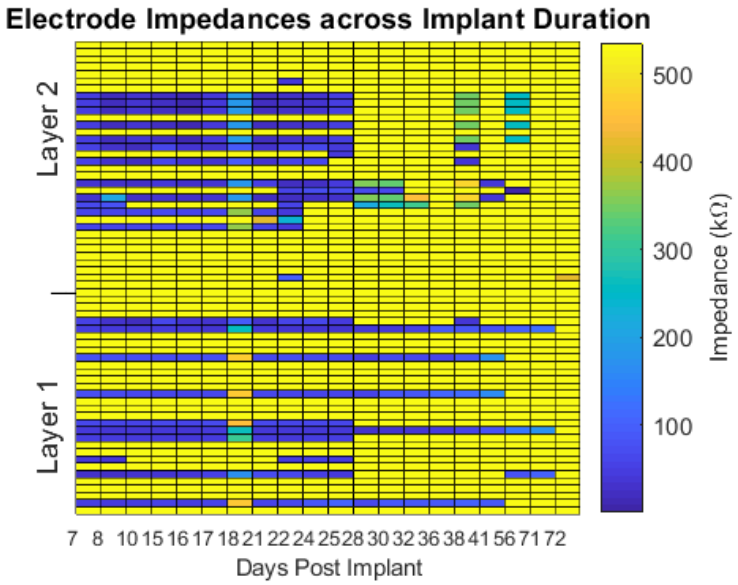

Figure 2.12. Electrode Impedances across Implant Duration. Rows correspond to electrodes and columns represent recording sessions. 10 electrodes in layer 1 and 17 electrodes in layer 2 registered impedances beneath the 536 kOhm device cutoff on at least one session. A connection issue manifested 28 days post implant, although no interruption in recorded signals was observed at this time.

Recording Characteristics. The recordings taken from the implanted bilayer array in the 3rd feline implant qualitatively showed increased amplitude in the mid-spectrum areas relative to a straight-line slope in 1/f scaling. This structure is apparent as a mid-spectrum "knee" or change in slope (Figure 2.13, left), similar to data recorded in a separate experiment from a conventional PMT µECoG array implanted over human cortex (Kellis, 2010). This mid-spectrum structure typical of cortical surface potentials (Miller, 2009) was observed on both layers of the bilayer array. An example recording taken 22 days post implant showed no statistically significant differences (Wilcoxon rank-sum test,

p > .05 in all comparisons) in mean spectrum amplitude in any frequency band between viable electrodes from layers 1 and viable electrodes from layer 2 (Figure 2.13, right).

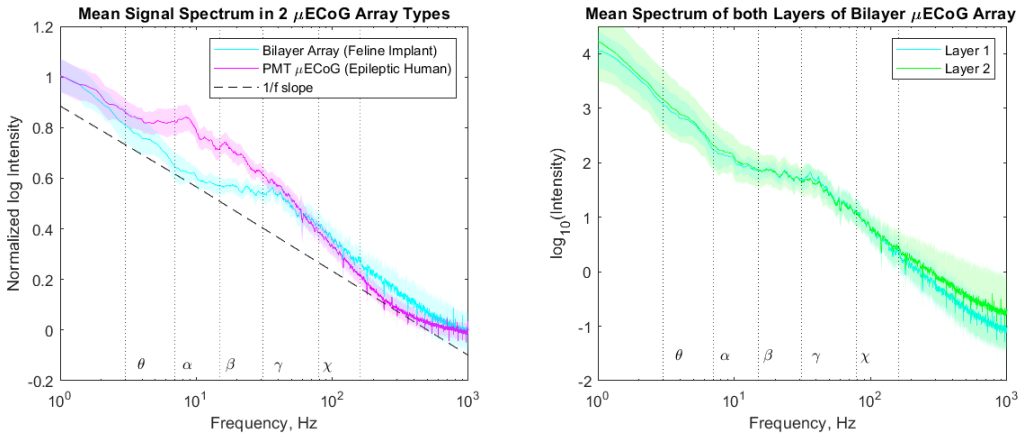

Figure 2.13. Mean spectra of sample LFP recordings. Spectrums of recordings were averaged across electrodes and further sampled from non-overlapping time windows. Shaded area represents ± 1 standard deviation. Data from the bilayer array were collected 22 days post-implant. Left, normalized mean spectrum from viable electrodes on layer 1 of the bilayer µECoG array in a feline implant (cyan) are plotted along with mean spectrum from electrodes on a conventional PMT µECoG array implanted over cortex in a human with epilepsy (magenta) as a reference. Spectrums from both µECoG types show a mid-spectrum "knee" from change in log-scale slope, typical of cortical surface signals (Miller, 2009). Right, mean spectrum from electrodes on layer 1 of the bilayer array (cyan) is shown with mean spectrum from electrodes on layer 2 (green). No significant differences in mean spectrum amplitude between Layer 1 and Layer 2 were observed in any of the frequency bands (Wilcoxon rank-sum test, p > .05 for all comparisons).

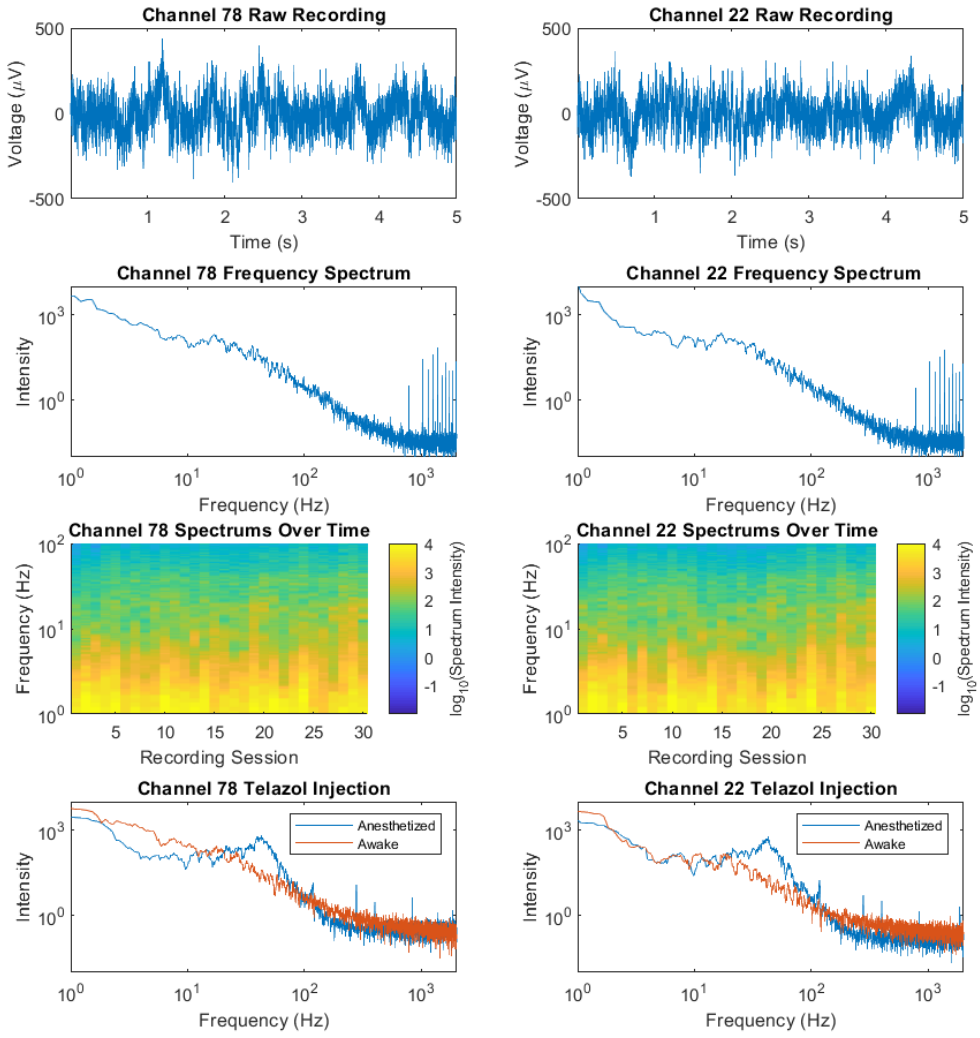

Figure 2.14. Representative Recordings from Both Layers. Left column contains plots for an electrode from Layer 1 (channel 78), while right column contains plots for an electrode from Layer 2 (channel 22). Top row shows 5 second recordings of continuous data for each electrode. Second row shows frequency spectrum from multi-taper spectral estimate of each 5 second recording. The 3rd row shows heat maps of spectrums from each recording session across implant duration. The 4th row shows spectrums from awake and anesthetized state after Telazol injection in experiment #1 (22 days post-implant).

Despite the improvements to electrode impedance in the 3rd iteration array, cortical stimulation experiments were still unsuccessful in evoking muscle twitches in the anesthetized feline. In order to further validate a neural origin of the recorded signals in the absence of successful stimulation, the response of recorded signals to induction of general anesthesia via Telazol injection was analyzed for both layers of the array. Frequency spectrums from electrodes in both layers showed robust, frequency band-dependent modulation in recordings taken 1 hour after induction of anesthesia via Telazol injection, and the modulation consistently occurred in three separate experiments taking place 22 days post-implant, 44 days post-implant, and 73 days post-implant (Figure 2.15). The frequency-band-dependent modulation included a large increase in amplitude in the beta and gamma frequency bands and decreased amplitude in theta band for both layers in all 3 experiments, with spectrum crossovers occurring in alpha and chi bands. The spectrum amplitude changes observed in theta, beta and gamma bands were statistically significant for both layers in all three experiments (Wilcoxon signed-rank paired difference test at $\alpha = .05$; amplitude change and significance summarized in Table 2.1). The distributions of spectrum amplitude change in each frequency band were often similar for layer 1 and layer 2; a Wilcoxon rank-sum test failed to reject the null hypothesis of different distributions of Telazol-induced change at $\alpha = .05$ in 9 of 18 total comparisons for layer 1 vs layer 2 (summary in Table 2.2). In addition to the change in spectrum amplitude in the five analyzed LFP bands, a decrease in spectrum amplitude was observed to extend until the noise floor, as high as 1-2 kHz.

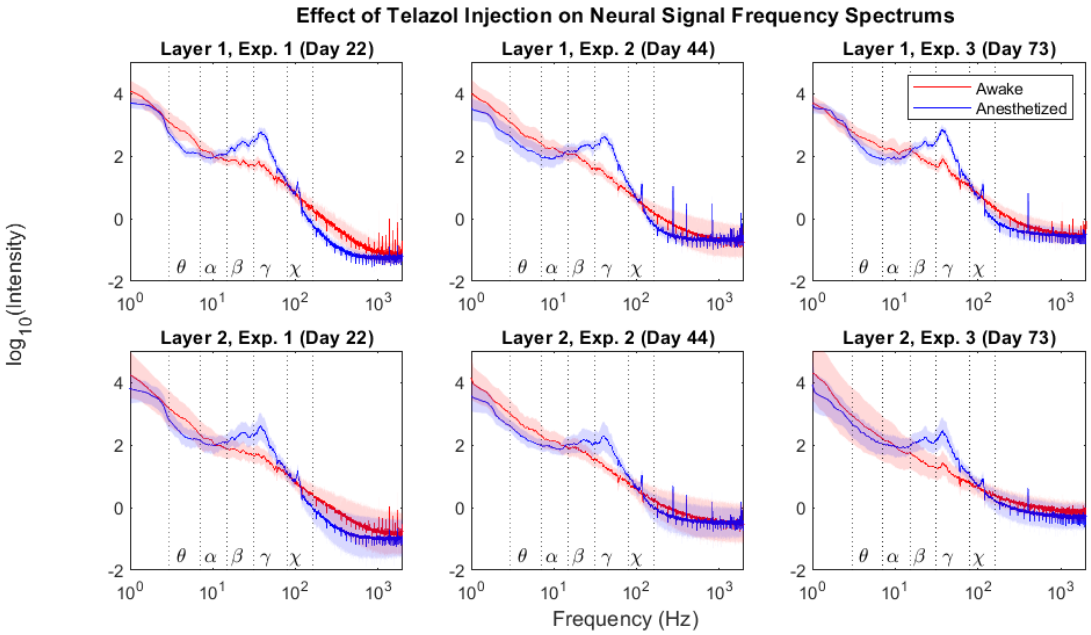

Figure 2.15. Effect of Telazol on Frequency Spectrums. Top row shows spectrums of signals recorded from viable electrodes in Layer 1, while bottom row shows spectrums from viable electrodes in Layer 2. Solid line represents mean spectrum across viable electrodes, with shaded area at 1 standard deviation. Red spectrums are from the awake state prior to induction of general anesthesia via Telazol injection, while blue spectrums are from the anesthetized state roughly 1 hour post injection. Induction of anesthesia was replicated across 3 experiments, corresponding to plot columns. Spectrums from both layers in all experiments consistently showed a large, significant increase in amplitude in the beta and gamma frequency bands, with decreased amplitude in theta band and spectrum crossovers occurring in alpha and chi bands. Summary of statistical comparisons of awake vs anesthetized state for separate layers using Wilcoxon signed-rank paired difference test in Table 2.1; summary of statistical comparisons of differences in Telazol-induced change between layer 1 vs layer 2 spectrums using Wilcoxon rank-sum test in Table 2.2.

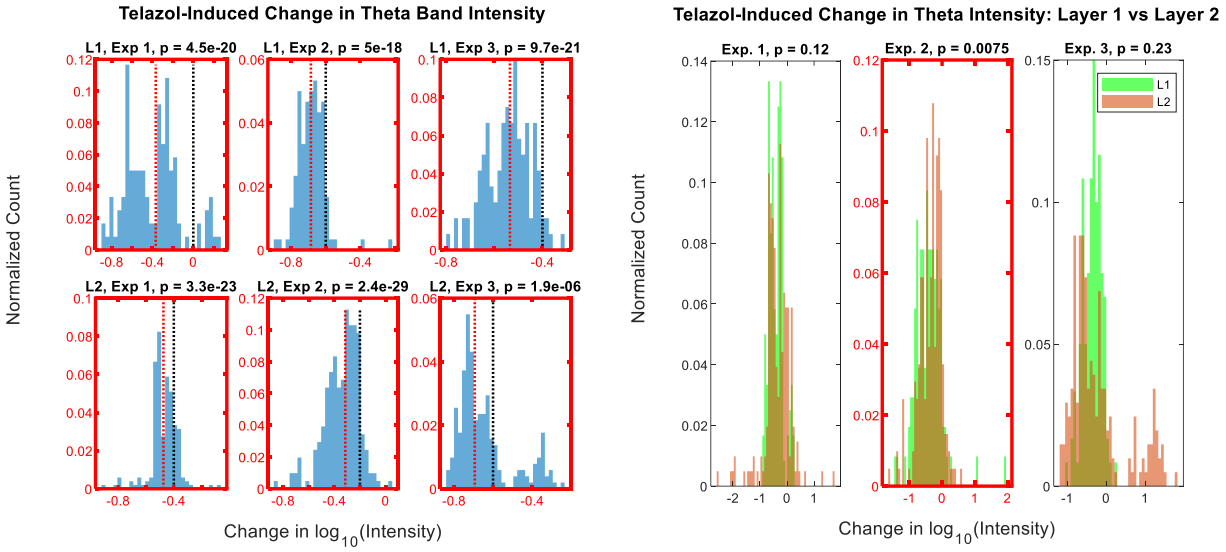

Figure 2.16. Comparison of Distributions of Telazol-Induced Change in Intensity**.** Results are shown for an example frequency band (Theta, 4-7 Hz). Spectrums were calculated for all viable electrodes in each layer during 12 non-overlapping, 5-second time segments for awake and anesthetized conditions. Left, distributions of mean spectrum change in theta band from the awake state to the anesthetized state are shown for layer 1 (top row) and layer 2 (bottom row) in 3 anesthesia induction experiments (columns 1 – 3). Red dotted line marks distribution median change, with the black dotted line at 0 change. Each distribution was tested against no change in a Wilcoxon signed-rank paired difference test (complete results in Table 3), with significance indicated by bold red axes. Right, distributions of mean spectrum change in theta band for layer 1 (green) and layer 2 (brown) are superimposed for each experiment. The layer distributions were compared in a Wilcoxon rank-sum test (complete results in Table 2), with significantly different distributions indicated by bold red axes.

Table 2.1. Statistical Comparison of Awake vs Anesthetized States. Telazol-induced change in mean spectral power is shown by frequency band, layer and experiment number. The median change in mean spectral power and the p-value for the corresponding Wilcoxon signed-rank paired difference test (vs no change) are reported for each frequency band, layer of bilayer μECoG array, and experiment (induction of general anesthesia via Telazol injection). Asterisk indicates significance vs null hypothesis of no change at $\alpha = .05$ (p-value of .0083 with Bonferroni correction for 6 comparisons per frequency band).

		θ Band (3-8 Hz)		α Band (7-16 Hz)		β Band (15-32 Hz)		γ Band (31-80 Hz)		χ Band (79-161 Hz)		High Freq (250-1000 Hz)	
		median change	p-value	median change	p-value	median change	p-value	median change	p-value	median change	p-value	median change	p-value
Layer 1	Exp. 1	-0.37	4.5e-20 *	0.021	0.07	0.56	2e-21 *	0.58	2e-21 *	-0.17	8.9e-08 *	-0.23	2e-21 *
	Exp. 2	-0.43	5e-18 *	-0.15	6.4e-11 *	0.42	2e-21 *	0.71	2e-21 *	-0.036	0.051	-0.062	0.023
	Exp. 3	-0.34	9.7e-21 *	-0.19	1.1e-14 *	0.48	2e-21 *	0.54	2e-21 *	-0.19	9.2e-16 *	-0.08	2.8e-08 *
Layer 2	Exp. 1	-0.37	3.3e-23 *	0.032	0.0028 *	0.54	9.9e-31 *	0.51	9.5e-34 *	-0.12	2.6e-08 *	-0.21	5.4e-31 *
	Exp. 2	-0.29	2.4e-29 *	-0.095	1.2e-11 *	0.31	1.7e-31 *	0.67	3.6e-34 *	0.034	0.0081 *	0.013	0.83
	Exp. 3	-0.47	1.9e-06 *	-0.072	0.034	0.71	1.6e-33 *	0.64	2.7e-34 *	0.015	0.044	-0.29	3.1e-22 *

Table 2.2. Comparison of Telazol Effect across Layers. Difference in Telazol-induced change of mean spectral power in layer 1 vs layer 2 is shown for each experiment. The p-value for the Wilcoxon rank-sum test for difference in distributions of mean Telazol-induced change for layer 2 vs layer 1 electrodes is reported along with the corresponding difference in median change of mean spectral power. Asterisk indicates significance vs null hypothesis of equal distributions at $\alpha = .05$ (p-value of .0167 with Bonferroni correction for three comparisons per frequency band).

	θ Band (3-8 Hz)		α Band (7-16 Hz)		β Band (15-32 Hz)		γ Band (31-80 Hz)		χ Band (79-161 Hz)		High Freq. (250-1000 Hz)	
	Diff. in median Δ	p-value	Diff. in median Δ	p-value	Diff. in median Δ	p-value	Diff. in median Δ	p-value	Diff. in median Δ	p-value	Diff. in median Δ	p-value
Exp.1	-0.0053	0.12	0.011	0.48	-0.016	0.16	-0.074	0.00018 *	0.046	0.15	0.013	0.19
Exp.2	0.14	0.0075 *	0.055	0.048	-0.11	0.00052 *	-0.044	6.7e-05 *	0.07	0.00024 *	0.075	0.33
Exp.3	-0.13	0.23	0.12	0.00024 *	0.23	0.0019 *	0.1	0.072	0.2	6.5e-15 *	-0.21	0.00042 *

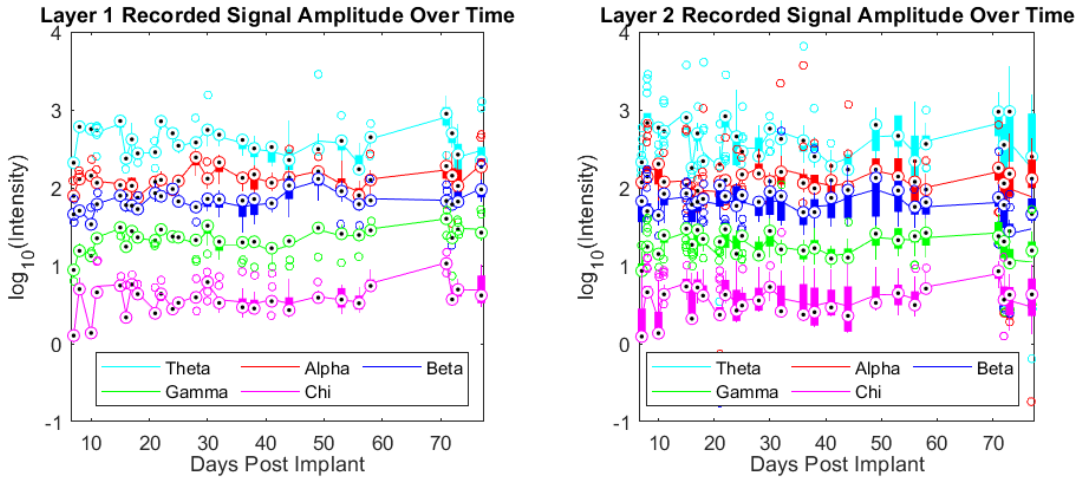

Figure 2.17. Longitudinal Signal Amplitude. For each frequency band, boxplots are shown for each recording with connecting line at median value for all viable electrodes in layer 1 (left) and in layer 2 (right). Linear regressions were calculated for each frequency band using a Linear Hypothesis Test vs a flat slope (complete results in Table 2.2). No significant negative trends were detected for any frequency bands on either layer at $\alpha = .05$.

Spectrum amplitude was stable in each frequency band across recording sessions spanning 77 days. Linear hypothesis testing did not find any significant negative trends in any frequency band at $\alpha = .05$. Figure 2.17 provides a visualization of longitudinal spectrum amplitude by frequency band, while Table 2.2 summarizes linear regression output and significance.

DISCUSSION

A new design was demonstrated for a flexible µECoG array with bilayer routing on a PDMS substrate. Both layers yielded electrodes that were capable of recording

neural signals of similar amplitude and frequency content from the cortical surface, with stable amplitudes across all frequency bands for 77 days post-implant. The mid-spectrum "knee" observed in the frequency spectrums of electrodes from both layers is characteristic of field potentials recorded from the surface of the brain across a variety of factors, including cortical area and local neural activity, and is reflective of underlying synchronized oscillations of neural tissue (Miller, 2009).

Despite improvements to electrode impedance and the success of *in vitro* stimulation testing in saline prior to implant, the 3rd generation array was still unsuccessful in eliciting muscle twitches through epicortical stimulation. One possible reason for this is that the minority of electrodes that could register valid impedances might not have been over the correct motor areas of the cortex. Putative sensorimotor areas in feline cortex are in the anterior portions of the brain (Figure 2.2), unlike the more centrally located sensorimotor cortical areas in humans and nonhuman primates, due to a comparatively small prefrontal lobe. The overlap between array placement and the most anterior-medial portion of the array presents a small target that may have been largely missed. It is also possible that any electrodes that did cover this region may still not have been sufficiently low in impedance for effective stimulation, particularly given the drop in test output amplitude that occurred after the assembly was physically manipulated for the pedestal mount (Figure 2.7 and Figure 2.8). A study using similarly sized electrodes implanted in awake Rhesus Macaques to elicit visual percepts via epicortical micro-stimulation found effective stimulation amplitudes were in the range of 300 µA (Oswalt, 2016). The TDT IZ2 stimulator used in both studies limits stimulation voltage to 12 V, allowing 300 µA only on electrodes of 40 kOhm or less. Of the five channels in the lower left corner

targeting motor cortex that continued to show high stimulation amplitude after the second pedestal mount (ch. 31, 48, 34, 26, 40), none registered impedances less than 50 kOhm in the implanted array. Many other electrodes registered impedances below 40 kOhms, and stimulus artifact from the cortical array was observed in fine-wire EMG electrodes in the hind limb even when no muscle twitches were evoked. Given these observations, it may be possible that the arrays in this study were indeed passing current into the body, but only at subthreshold levels, or in cortical areas less likely to evoke muscle twitches when stimulated.

Roughly half of the electrodes on the array did not register valid impedances beneath the TDT PZ5 cutoff of 536 kOhm. It is possible that this is a consequence of the methods used to connect the bilayer array to the PCB and recording hardware, rather than a direct consequence of the bilayer routing technique. When the PCB assembly was physically manipulated or bent during pedestal mount, many channels were observed to have substantial reduction in stimulation output amplitude. However, not only did many of these channels regain capacity for stimulation when the array was unmounted, but some previously low amplitude channels actually experienced increased amplitude when the PCB assembly was again handled and attached to the pedestal. These observations are in line with inconsistent or unstable connections between the wire contact sites on the PDMS substrate and the contact sites on the compression-bound PCB layers. It is possible that an alternate method of connecting the wire traces to a head stage, rather than compression bonding with silver paste, could result in more channels with low impedances and potentially resolve the shorting between channels as well.

Although successful stimulation was not demonstrated for the device, the signals recorded through the duration of the implant are indicative of a neural origin on both layers of the array, suggesting successful recording capabilities of the novel bilayer routing method. Electrodes from both layers were also able to consistently record frequency-dependent signal modulation induced by general anesthesia via Telazol injection. While anesthesia has been often been assumed to generally suppress brain activity (Friedman 2010), recent studies have indicated that anesthetic agents may actually modulate the dynamics of broad neuronal networks (Cimenser 2011, Lewis 2012). The effect of different anesthetic agents on mesoscopic-scale LFP dynamics, such as those recorded by μECoG arrays, has not been widely studied. However, recent studies have found that anesthetic modulation of local field potentials may differ by cortical area and layer, with anesthesia by isoflurane inducing frequency-specific peaks in V1 visual cortex, and broadband enhancement of LFP power in wide areas of prefrontal cortex in ferrets (Sellers 2013). The emergent recovery state from general anesthesia has been observed to generate neural activity with different dynamics from loss of consciousness or sleep, thought to be part of a possible "boot-up" sequence driven by ascending arousal centers (Flores 2017; Lewis 2018). One feature that has been observed during the emergent state is elevated 10-40 Hz power across a broad cortical region (Lewis 2018). The broad increase in power in beta and gamma bands observed in this study (~15-80 Hz) may be part of a similar emergent network dynamic phenomenon. Anesthesia by propofol in cats has been shown to occur with reduced action potential firing (Hanrahan 2013). As high gamma and some broadband spectrum changes have been linked to local action potential firing (Manning, 2009; Ray, 2011; Miller, 2014), the decrease seen in this study as high as 1 kHz may be

related to a decrease in action potential firing caused by anesthesia. Differences in frequency-specific modulation among studies may be due to differences such as anesthetic agent, model species, cortical region, and the scale and specificity of signals recorded by different devices. Regardless of specific network dynamics, the robust presence of frequency-specific modulation of the recorded signal in this study upon induction of anesthesia is likely indicative of a neural origin of the recorded signals from electrodes in both layers.

Chapter 3

DETECTION AND USAGE OF HIGH FREQUENCY FEATURES OF NEURAL ACTIVITY IN A SPEECH DECODING ALGORITHM

ABSTRACT

While non-penetrating surface electrodes tend to provide recording longevity and minimal tissue response, penetrating electrodes must normally be used to detect and isolate individual action potentials from cortical neurons. However, general spiking activity may contribute to increased energy from 300 - 6000 Hz in the frequency spectrum. Recently, surface electrodes have been developed that were able to record isolated spikes with features of superficial cortical neurons (Khodagholy, 2015). Here, data were re-examined that had previously been recorded from subdural micro-electrocorticography (µECoG) arrays implanted in a human patient over the face-motor cortex, which is associated with direct production of speech, and over Wernicke's area, which is associated with the comprehension and processing of language. Classification of spoken words had previously been achieved by decoding local field potential (LFP) data recorded from these arrays (Kellis, 2010). The study in this chapter found that several channels exhibited a consistent increase in frequency spectrum energy extending as high as 2 kHz, well above classically recognized LFP bandlimited components and potentially indicating action potential (AP) spiking activity. The amount of increases in high frequency power differed across electrode and word pairs, providing a descriptive feature set for classification algorithms. A K-Nearest Neighbor classifier algorithm was used to predict spoken words from high

frequency spectral power increases with 94.5% accuracy, indicating the presence of informative neural activity from 250-2000 Hz recorded from surface µECoG electrodes that may potentially reflect features of AP firing in local neuronal populations.

INTRODUCTION

Several factors generally prevent the detection of action potential waveforms from nonpenetrating surface electrodes. Currently available conventional surface micro-Electrocorticography (µECoG) arrays fail to conform to the curved cortical surface, and their electrodes record the aggregate activity of relatively large neuronal populations due to the electrode size and distance from cortical neurons (Miller, 2009b). However, while individual waveforms from action potentials are typically not resolvable from surface recordings, neuronal spiking correlates with a broadband (0-200 Hz) increase in local field potential (LFP) power (Manning, 2009; Ray, 2011; Miller, 2014). Additionally, the high gamma band (~60-150 Hz) of LFP recordings has been hypothesized to include components of firing from nearby neurons, including neurons too distant from the microelectrode to have resolvable waveforms (Ray, 2011).

The amplitude of extracellular potentials in the brain tends to decrease with frequency as described by an inverse power law (Miller, 2009a). The particularly high amplitude and spatial reach of low-frequency LFP signals is largely thought to be due to synchrony and resonance in the aggregate oscillations of postsynaptic potentials from many neurons, while higher frequency content is believed to be less synchronous and more localized. Some studies have proposed that the lower spatial reach of high frequency signals is due to biophysically based low pass filtering in cortical tissue caused by

capacitive properties of neural tissue (Bedard, 2004). However, direct in vivo testing of impedance characteristics of neural tissue in Macaques indicates purely resistive properties, regardless of frequency or direction or depth of measurement. (Logothetis, 2007). Broadband spectral increase during task onset has been noted to sometimes lack a definitive upper bound (Miller, 2014), and this broadband signal is sometimes extracted up to around 200 Hz with with the assumption that this captures the majority of the variance associated with asynchronous neuronal spiking. However, frequency spectrums of individual action potentials show peaks in intensity at frequencies from 400 Hz to 1+ kHz, and the spectrums of longer recordings containing these action potentials show clear activity in these frequency bands (Figure 3.1). A recent study analyzing wavelet decomposition of neural features in different frequency bands of recordings from penetrating microelectrodes found both greater stability and information density in mean wavelet power from 234-3750 Hz compared to voltage threshold techniques for multi-unit activity, up to 3 years post-implant (Zhang, 2018). Given these observations, it is possible that recordings taken from surface μECoG arrays may also include high-frequency features of neuronal action potential activity in the hundreds or even thousands of Hz. Recently, action potential waveforms were even isolated from recordings taken from the cortical surface using a novel, conformable array with micro-scale (10 μm length) electrodes (Khodagholy, 2015).

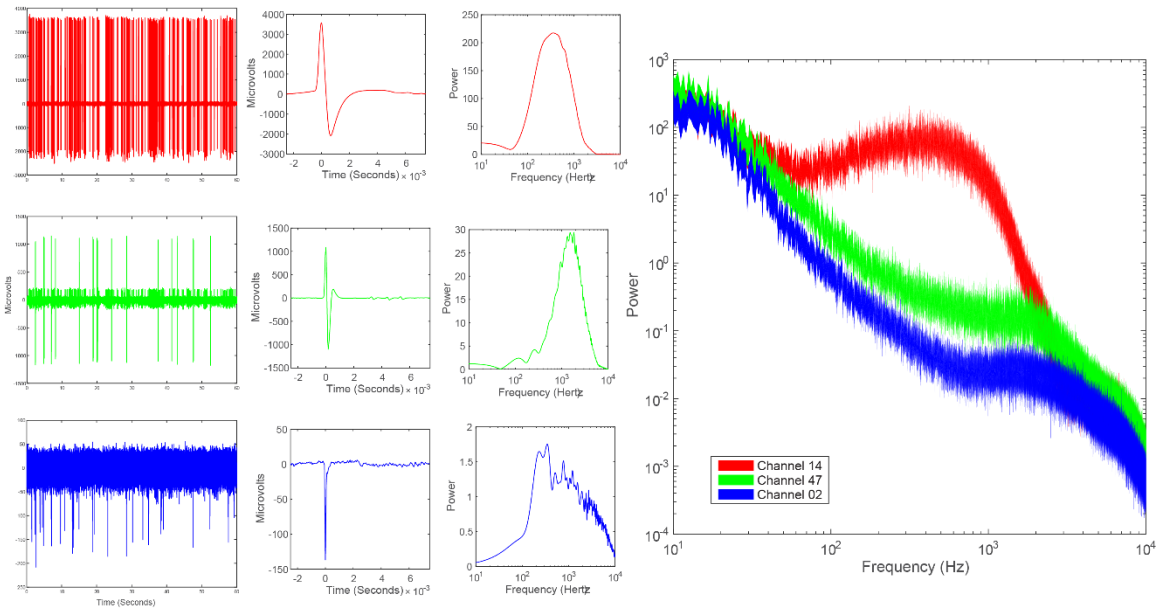

Figure 3.1. Action Potential Spectrums. Multi-taper power spectral density estimates are shown for isolated, single action potentials recorded in another study (Baker 2009; Egan 2012) from penetrating microelectrodes. Peak spectral power of single action potential waveforms is observed at frequencies from 400 Hz to 1+ kHz depending on action potential waveform shape and duration. Right, spectra of 1-minute recordings containing the respective action potentials show increased amplitude in frequency ranges similar to the peaks of the corresponding AP waveforms.

Penetrating intracortical microelectrode arrays are typically used when recordings containing isolatable action potential waveforms from single neurons are desired, but these devices introduce several problems by piercing the pial surface. Chronic implantations can lead to persistent tissue inflammation and possible encapsulation of electrode tips by glial cells (Polikov, 2005), which may play a role in the loss of signal amplitude and number of viable channels often observed on a timescale of 6-12 months (Ryu, 2009). Analysis of

the very high frequency bands corresponding to the highest amplitude spectral peaks of action potential waveforms could potentially provide a more direct measure of neuronal spiking than the surrogate measure provided by the high gamma band. Improved detection of neuronal spiking activity from µECoG arrays would impart a degree of the signal specificity inherent to intracortical electrode arrays without requiring their invasiveness. This could potentially open a new category of neural signal information to applications in neuroprosthetics or clinical monitoring that are constrained to surface electrodes for reasons of safety or longevity.

This study examined very high frequency (250-2000 Hz) components of recordings previously taken from subdural µECoG arrays implanted in a human patient over the face-motor cortex and Wernicke's area in order to extract a descriptive feature set for speech classification algorithms. Wernicke's area is associated with the processing and comprehension of both spoken and written language, while the face-motor cortex is involved in the direct, mechanical control of articulation of words (Terao 2007). LFP signals taken from the arrays over these areas had previously been used to predict words spoken by the patient in this study (Kellis, 2010). To validate the presence of informative, high-frequency features of neuronal activity in the same recordings, a K-Nearest Neighbor classification algorithm was used with only high-frequency content as input to demonstrate proof of concept.

METHODS

Experimental setup and data collection: A human subject undergoing extraoperative ECoG monitoring for refractory epilepsy had two µECoG arrays implanted subdurally over face-motor cortex and Wernicke's area (Figure 3.2). Recording sites in each microelectrode array (PMT Neurosurgical, Chanhassen, MN) were formed from the terminations of 40-µm diameter wires arranged in a 4x4 grid with 1 mm spacing. A list of ten words was selected: "yes", "no", "hot", "cold", "hungry", "thirsty", "hello", "goodbye", "more", and "less". The patient was instructed to repeatedly articulate each word, with a visual cue to speak given approximately 1 second after the end of each repetition. Data from the µECoG arrays were bandpass filtered from .3-7500 Hz and sampled at 30 kHz.

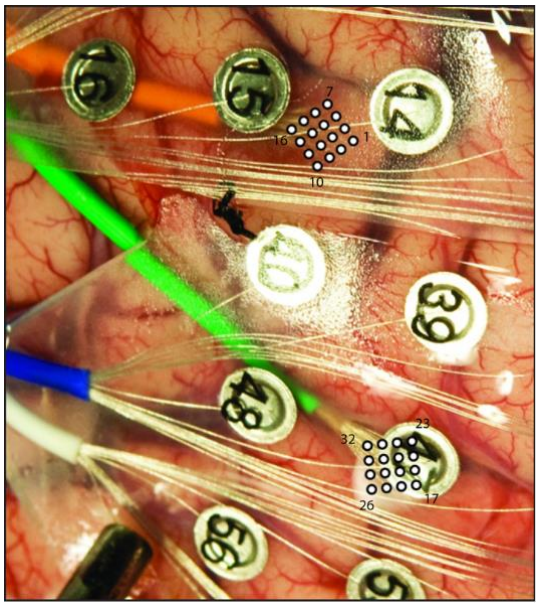

Figure 3.2. Placement of µECoG Array over Cortical Speech Areas**.** Two µECog arrays were subdurally implanted in conjunction with a macro-scale ECoG array used for clinical epilepsy monitoring. One array was placed over Wernicke's area, associated with language processing, while the other was placed over face-motor cortex.

Feature extraction: Initially, to ascertain the presence of informative, decodable content in the frequency band from 250-2000 Hz, spectrums were calculated for the recording segments from -0.25 s to +0.5 s relative to speech onset for each spoken word. Spectrums were also calculated from the 0.75 s recording segments immediately preceding each spoken work. Mean frequency spectrum change during spoken word production was computed by dividing the trial spectrums by the preceding period spectrograms, elementwise across frequency bins, and averaging across trials.

Afterwards, to generate a time-varying signal from the high-frequency components of the recordings suitable for use in a decoding algorithm, spectrograms were generated from the signals using a 0.5 s window and a 0.05 s step size, or spectrum sampling at 20 Hz. A multi-taper windowing function was used with a time bandwidth product of 9. As high frequency components of neural recordings drop off quickly due to power-law scaling (Miller, 2009), the spectrograms for each channel were normalized with respect to the mean spectrum for that channel across the recording. This frequency normalization may help prevent the intrinsically higher amplitude low frequency components from dwarfing the activity in higher frequencies in a given frequency band. The resulting normalized time-frequency matrix was averaged over frequency bins in the 250-2000 Hz range to create a time-varying, instantaneous measurement of high-frequency spectral power for each channel.

Feature evaluation in a speech classification algorithm: A simple classification algorithm, Gaussian kernel weighted k-nearest neighbor (KNN) classification, was used to decode spoken words from the instantaneous high-frequency spectral power index from all

32 channels across the two implanted μECoG arrays. KNN is a simple supervised learning method, i.e. an algorithm with a distinct training phase to form a hypothesis to map inputs to outputs, that can be applied in both classification and regression problems. For every point in time, sampled at 20 Hz, the estimates of instantaneous, frequency-normalized, mean spectral power from 250-2000 Hz were taken from every channel and used as inputs to the KNN classifier, with the ten spoken words and the baseline inter-trial interval forming 11 output categories. In the training phase of the algorithm, high-frequency feature vectors of the training examples were stored along with their output word category. In the test phase, when predicting a test instance for a given time sample, the mode of the class labels of the k nearest neighbors in feature space was the output for classification. An exhaustive search method was used when locating nearest samples. The KNN algorithm in this study used a standardized Euclidean distance metric to the 15 nearest training samples. A Gaussian kernel operator gave increased weight to training samples based on proximity to the test sample by the equation:

$$K(d) = \exp\left(-\frac{d^2}{2\sigma^2}\right)$$

where *d* represents the Standardized Euclidean Distance, and σ was set to 15. Data points for training and testing were sampled at the reciprocal of the spectrogram moving window step size, or 20 Hz. The data points from -0.25 s to +0.5 s relative to the markers for speech onset were assigned to the word spoken during that window, with all other data points assigned to the inter-trial interval category. A 10-fold cross-validation was used to assess the KNN classifier accuracy, with one test fold and nine training folds for each iteration. Classification accuracies above chance indicate the detection and utilization of

behaviorally pertinent features of high-frequency neuronal communication instead of stochastic physiological data.

RESULTS

Spectrums of .75 second recording segments taken during speech production showed frequency-dependent amplitude differences compared to spectrums of recording segments during preceding periods, including a broadband increase in power extending as high as 2 kHz for some electrodes and words. (Figure 3.3). The relative change in the speech spectrum compared to the silent spectrum, averaged across trials, could similarly show a broad increase across frequencies that peaked in high gamma (~100 Hz) but continued to 2 kHz with possible additional small peaks around 400 Hz and above 1 kHz.

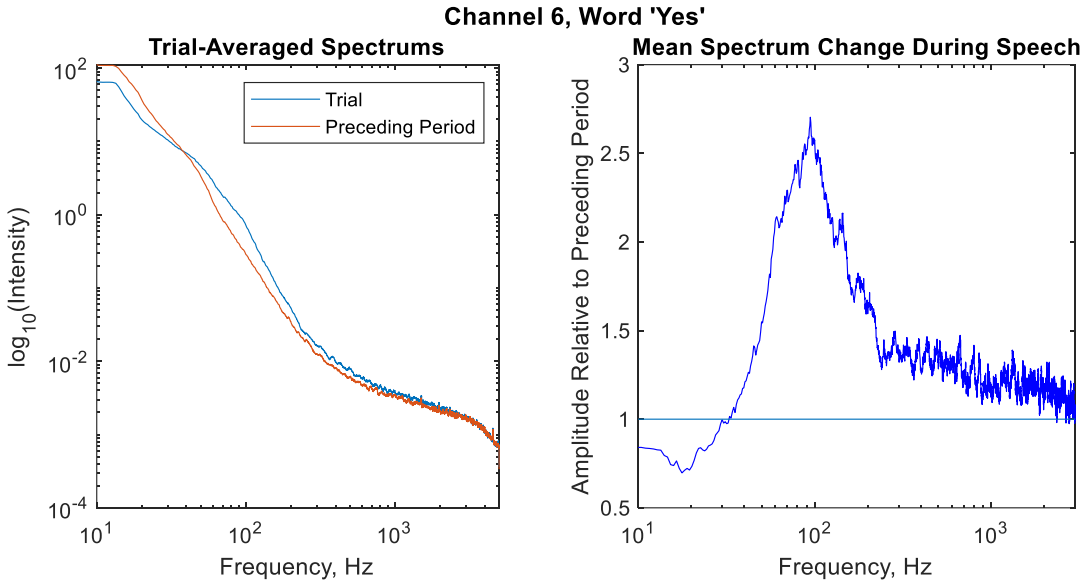

Figure 3.3. Frequency Spectrum Change During Speech. Data are from a representative electrode from the µECoG grid implanted subdurally over face-motor cortex. Left, trial-

averaged (n = 51) spectrums are shown for .75 s recording segments extracted from -0.25 s to +0.5 s relative to onset of speech during trials of production of the word “Yes”, and for segments extracted from the immediately preceding, silent baseline period. In addition to the patterns of LFP activity below 200 Hz, a small but consistent increase in power during speech trials is visible as high as 2 kHz. Right, the relative spectrum change from baseline is averaged across trials. Spectrum increase extends as high as 2kHz and shows possible peaks around 400 Hz and above 1 kHz.

Instantaneous mean spectral power from 250-2000 Hz, computed by averaging across frequency-normalized spectrograms, also showed strong modulation in amplitude relative to onset of speech trials for some channels and words (Figure 3.4 and Figure 3.5). Cortical high-frequency content recorded by electrodes over face-motor cortex showed a larger average increase in amplitude upon speech onset compared to electrodes over Wernicke’s area (Figure 3.6), which showed less increase in amplitude on average upon speech production. Electrodes over Wernicke’s area could additionally sometimes show increased high frequency activity during relaxed periods in between blocks of trials (Figure 3.5). Trial-Averaged change from baseline amplitude of instantaneous high frequency power showed distinct patterns across combinations of words and electrodes (Figure 3.7)

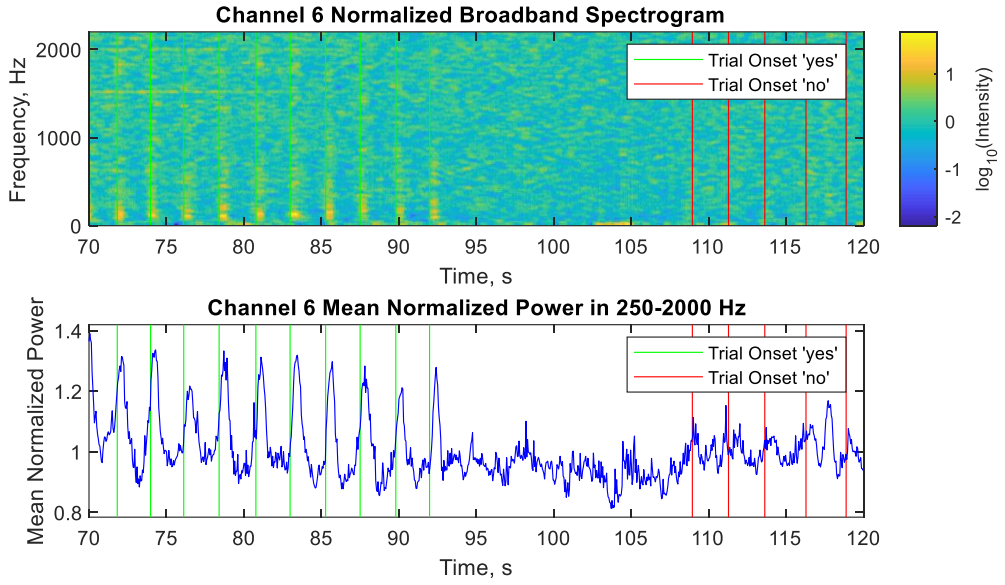

Figure 3.4. Instantaneous High Frequency Power from Face-Motor Cortex. Data are shown for an example electrode over face-motor cortex with preferential response for the word "Yes". Spectral power density normalized across frequencies, averaged from 250-2000 Hz, and calculated over time with a 0.5 s moving window shows robust amplitude variation with trial onset for "Yes" (green lines) but not for "No" (red lines).

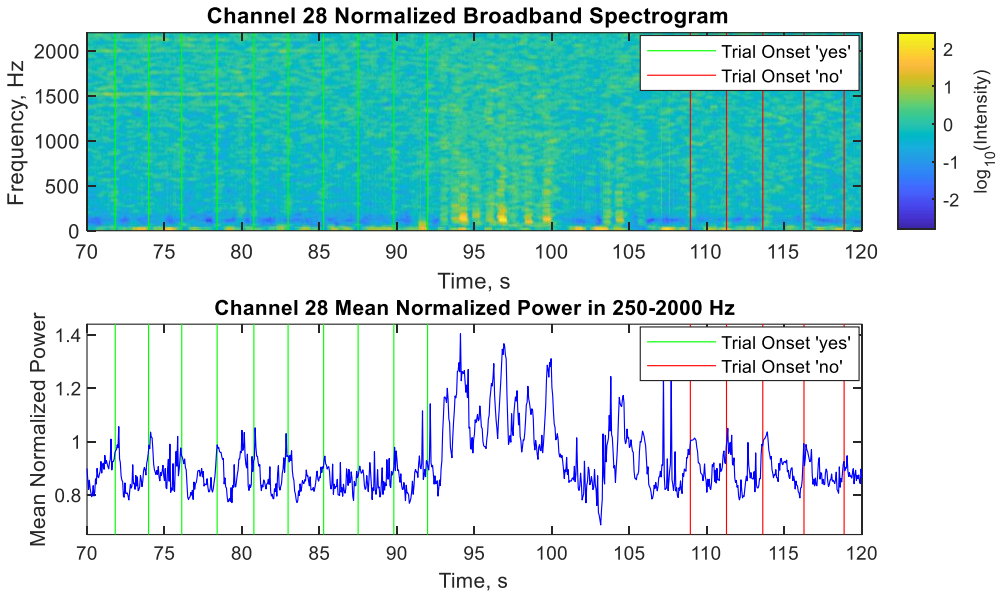

Figure 3.5. Instantaneous High Frequency Power from Wernicke's area. Data are shown for an example electrode over Wernicke's area with little preference exhibited for rote repetition of spoken trials of "Yes" or "No. Increased activity was observed during the longer breaks between blocks of trials and instructions.

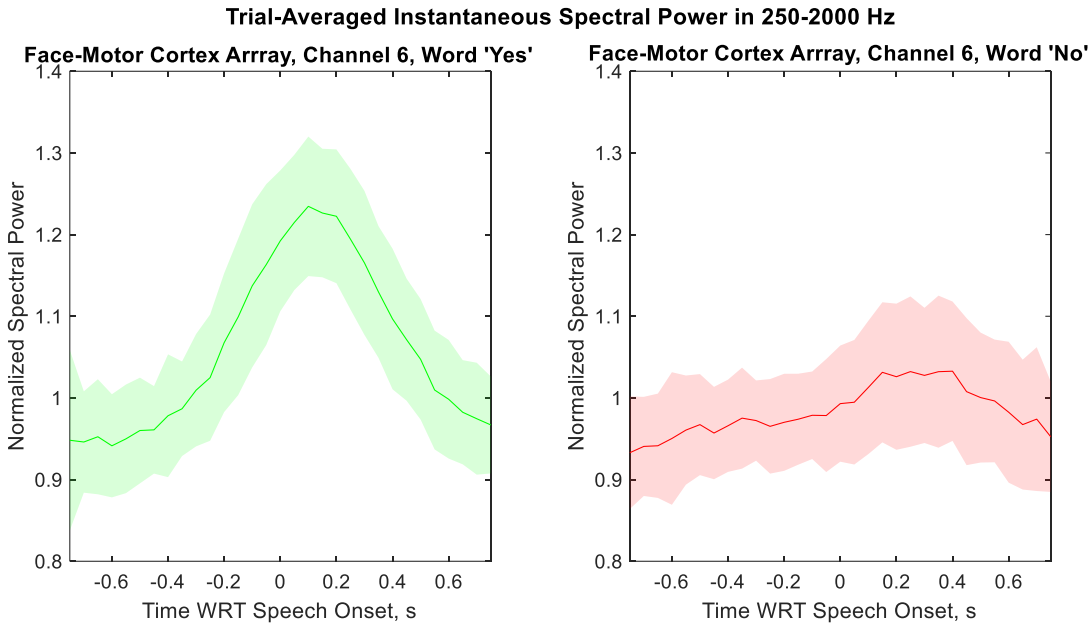

Figure 3.6. PSTHs of Instantaneous Spectral Power from 250-2000 Hz. Trial-Averaged, normalized spectral power over time provides a visualization of mean trends in cortical high-frequency neural activity relative to onset of speech production. Shaded region represents ± 1 standard deviation. Left, the preferential response of the example electrode for trials speaking "Yes". Right, the response of the same electrode relative to trials speaking "No" shows much weaker modulation.

Figure 3.7. Trial-Averaged High Frequency Modulation for all Words and Channels. Trial-averaged changes from baseline show distinct variation across different channel and word combinations. Electrodes 1-16 recorded from the array over face-motor cortex, while electrodes 17-32 recorded from the array over Wernicke's area

The K-Nearest Neighbor algorithm achieved an overall accuracy of 94.5 % in using instantaneous high frequency power from all electrodes to classify points in time as belonging to one of eleven speech classes. After 10-fold cross-validation, each word category was classified at 90% accuracy or higher, with the bulk of the error in distinguishing between speech and inter-trial intervals (Figure 3.8), compared to 9% accuracy expected by chance classification of data points from 11 categories.

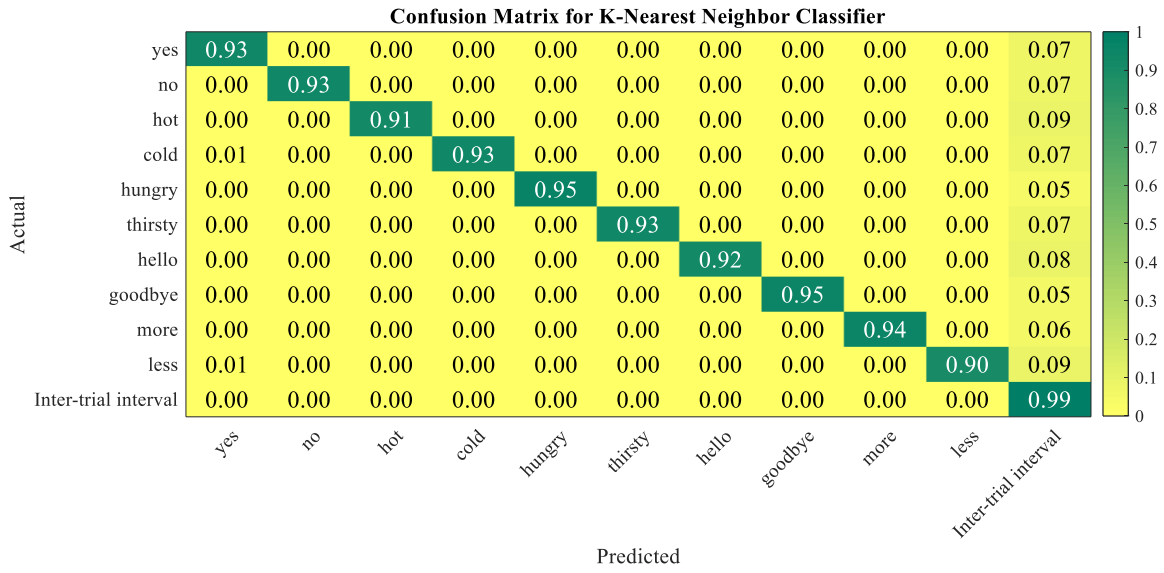

Figure 3.8. Classification Algorithm Results. A Gaussian kernel weighted k-nearest neighbor classifier with k=15 neighbors used the time-varying high-frequency spectral power mean from all electrodes to classify points continuously sampled in time as belonging to 11 speech classes (10 spoken words + inter-trial intervals). The above confusion matrix contains the cross-validated results from 10 fold validation. Overall classification accuracy was 94.5%.

DISCUSSION

The high-frequency features of neural activity recorded from subdural surface electrodes can provide a robust source of information correlating with spoken words. Though the high-frequency spectrum is much lower in amplitude than LFP signals, it exhibited a consistent relative change in power that varied across channel and word combinations, yielding an informative feature set for decoding and classification algorithms. Using this feature set, a Gaussian kernel weighted k-nearest neighbor classifier

was able to achieve 94.5% overall accuracy for 11 speech classes, compared to 9% expected by chance. This classification accuracy was for one day of recording during a speech task with one implanted patient, and is not directly comparable to previous classification results from this dataset as different metrics were used. Additionally, there were a limited number of trials; apart from "Yes" and "No", which had 51 and 45 trials, respectively, no other word had more than 10 repetitions. Nevertheless, success of a classification decode algorithm using only high frequency content from surface electrodes serves to establish a proof of concept that the frequency band of 250-2000 Hz may contain informative, decodable data even when recorded from nonpenetrating surface electrode arrays.

Frequency content in this high range has not typically been used in recordings from surface electrode arrays, and could thus potentially increase the amount of neural information available to such devices. However, there may be compromises as well. The advantages of neural interfaces utilizing surface electrode arrays include not just reduced tissue response and greater signal longevity compared to penetrating electrodes, but also lower requirements for bandwidth, computational speed, and battery life in designs for long-term implants, precisely because LFP signals can be sampled much more slowly than action potentials. The analysis of high frequency content from surface electrode arrays may thus forfeit one of their advantages in certain applications.

The high gamma band has been hypothesized to include components of firing from nearby neurons, including neurons too distant from the microelectrode to have resolvable waveforms (Ray 2011; Miller 2014). While the results of this study are consistent with contributions to the recorded surface signal from potentially more direct, higher frequency

components of action potential spiking, further work would be necessary to investigate the amount of independence between the 250-2000 Hz frequency band and the upper bands of LFP signals. However, since spoken words correlated with consistent changes in frequency spectrum power extending well beyond 1 kHz, action potential spiking activity near the surface electrodes might contribute to the high-frequency content of the recording, representing a source of information potentially distinct from LFP spectra and a generally useful signal for neural prostheses.

Chapter 4
DETECTION OF HIGH FREQUENCY FEATURES OF NEURAL ACTIVITY IN THE STUDY OF FUNCTIONAL CONNECTIVITY AND NEUROPATHOLOGY

ABSTRACT

Parkinson's Disease is associated with the disruption of normal function in cortico-basal ganglia – cortico loops, leading to various movement disorders. Electrophysiological recordings taken using macro-scale Electrocorticography electrodes have shown aberrant coupling between cortical regions and subcortical structures, such as between beta and gamma bands in deep basal ganglia structures and the primary motor cortex (de Hemptinne, 2013). Recordings taken using micro-electrocorticography (μECoG) electrodes may potentially characterize patterns of functional connectivity, or temporal correlations between spatially remote neurophysiological events, at a finer spatial scale. This study used μECoG arrays and penetrating FHC microelectrodes to investigate fine-scale functional connectivity between basal ganglia structures and areas of premotor cortex in patients with Parkinson's Disease. In addition to analysis of five classical local field potential (LFP) bands (Theta, Alpha, Beta, Gamma, and Chi), this study sought to detect patterns of functional connectivity in a high-frequency (250-2000 Hz) range matching the peaks in frequency content of action potential waveforms.

Spike-triggered averages (STAs) were computed between individual neurons in basal ganglia structures and cortical μECoG surface recordings using data from eight patients with Parkinson's disease who were undergoing standard clinical Deep Brain Stimulator (DBS) implantation. Time-frequency matrices were computed for the STAs, normalized by mean frequency spectrum, and averaged across each frequency band

separately. Peaks in spectral power, localized from roughly 800 -1600 Hz, were frequently observed in the STA waveforms. Significant spike-centered trends in these frequency bands relative to surrogate baseline activity generated from jittered spike times were detected in theta and alpha bands, and most commonly in the high frequency band. Overall, 19% of all basal ganglia neuron to cortical surface STAs exhibited significant trends in the 250-2000 Hz range, with power in this range peaking most frequently at 50 ms post spike time, compared to 40 ms pre-spike in Alpha band and 270 ms pre-spike in Theta band. These results indicate that patterns of functional connectivity in a frequency range high enough to match spectral peaks of action potential waveforms may be recorded using surface μECoG arrays. This technique may potentially provide a localized index of spike-to-spike communication between spatially discrete regions of neural tissue in the study of cortical function and neuropathology.

INTRODUCTION

Parkinson's Disease is a degenerative neurological disorder afflicting the motor system, associated with impairments such as bradykinesia, tremor, and impaired balance. The exact mechanisms causing these symptoms are unknown (Mink, 2003), but their progression is associated with the loss of dopaminergic cells in the Substantia Nigra. Parkinson's Disease is implicated in the disruption of normal function in cortico-basal ganglia – cortico loops (Lanciego, 2012). The Basal Ganglia are a system of subcortical nuclei situated at the base of the forebrain that form multiple parallel modulatory feedback loops with many wide areas of the cerebral cortex (Figure 4.1). These feedback systems

may contribute to movement selection, initiation, amplitude, and termination, as well as motor learning and the reward system of the brain. In the focusing model, the direct pathway permits activation of certain movement circuits by removing inhibition of thalamocortical cells, while the indirect pathway simultaneously suppresses various undesired movements through increased inhibition of related thalamocortical cells (Albin et al, 1989). This "center-surround" functional model does not explain the learning, reward-related, or habit formation functions of the basal ganglia, and it does not perfectly match basal ganglia structural anatomy. However, it is consistent with certain symptoms of movement pathologies such as those in Parkinson's Disease (Obeso, 2000), where cell death in the Substantia Nigra and the subsequent decrease in dopamine production may potentially result in reduced activity of the direct pathway and increased activity in the indirect pathway (DeLong, 1990; Obeso et al. 2000; Lanciego et al, 2012). This pathological interruption could impede movement amplitude at a given level of effort as well as movement selectivity.

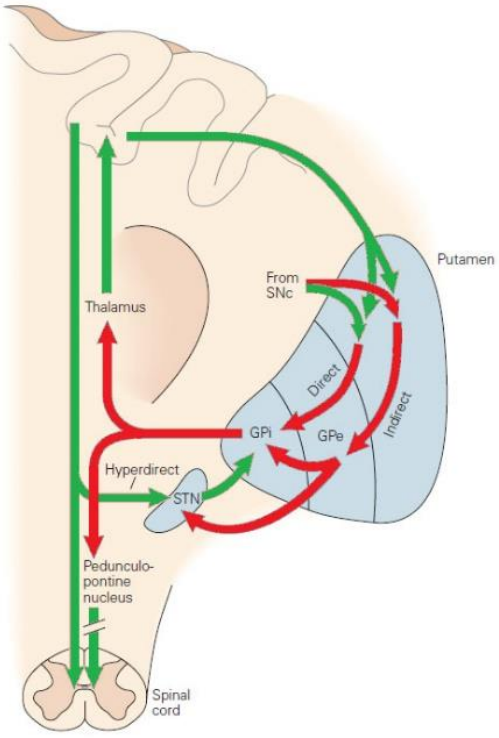

Figure 4.1. Basal Ganglia-Thalamocortical Circuits. Excitatory connections are shown in green, while inhibitory connections are shown in red. Image adapted from Kandel et al, 2013, Systems of Neural Science

Several pathological oscillations of neural signals are associated with Parkinson's Disease. Upon reduction of dopamine production, a pathological beta-band (12-30 Hz) oscillation appears in the cortex (Brown, 2007) and between the cortex and basal ganglia (Lalo, 2008). Patients with Parkinson's disease also exhibit prominent activity within STN in the beta band, which attenuates with dopaminergic treatment, while STN activity in the gamma (60-80 Hz) and theta (4-8 Hz) bands may increase. High-frequency oscillations (HFO, ~300 Hz) initially diminish with treatment, but can recover within minutes in a higher frequency range and with a more broad distribution (Lopez-Azcarate, 2010).

Dopaminergic therapy frees these HFOs from beta-band coupling, and their amplitude modulates with movement. Synchronization between neuronal action potential firing in STN and cortical field potentials recorded from primary motor cortex (M1) using macro-scale Electrocorticography (ECoG) electrodes (Shimamoto et al, 2013). Aberrant phase-amplitude coupling has also been observed in the Parkinsonian state between beta and gamma bands in deep basal ganglia structures and the primary motor cortex (de Hemptinne, 2012). In the healthy state, M1 broadband gamma activity displays phase modulation with low-frequency signals in a dynamic, task and site-specific manner. By contrast, excessive Parkinsonian phase-amplitude coupling may restrict the cortex to monotonous activity patterns that may disrupt its ability to respond to signals from other brain areas. This model possibly provides a basis for akinesia, a chief clinical sign of Parkinson's Disease. Deep brain stimulation can disrupt excessive cortico-subthalamic feedback and coupling patterns while simultaneously ameliorating some movement disorders associated with Parkinson's Disease.

Electrophysiological functional connectivity describes the temporal correlations between neurophysiological events that are spatially remote, regardless of any physical or anatomical connectivity that may or may not be apparent between them. The functional relationships between neural activity in basal ganglia structures and cortical neuronal populations may potentially be more precisely characterized through more localized and specific surface recordings. Neural recordings matching the cortical columnar scale of computation in the cerebral cortex may help identify new patterns of aberrant neuronal activity among different, smaller functionally coupled regions of the brain. The

aforementioned studies of cortico-basal ganglia synchronization typically recorded surface potentials from macro-scale, clinical ECoG grids, whose electrodes are millimeters in size and detect the aggregate activity of large neuronal populations. In contrast, micro-scale Electrocorticography (μECoG) arrays allow analysis of local field potential (LFP) signals at a millimeter to sub-mm scale, closer to the cortical columnar scale (Kellis 2016). This study employed μECoG arrays and penetrating FHC microelectrodes to investigate relationships between premotor cortical neuronal population activity and single neurons in basal ganglia in patients with Parkinson's Disease. The spike-triggered average (STA) of LFP signals is one method of detecting functional connectivity, assessing the strength of postsynaptic activity in a cortical region potentially affected by spiking in a different location (Jin 2008; Nauhaus 2009; Ray 2011).

In addition to recording a finer scale of cortical field potentials recorded, the smaller electrodes in μECoG arrays record from correspondingly smaller volumes of tissue, and consequently do not require as broad a degree of neuronal synchronization to achieve change in summed potentials (Kellis, 2016). The upper bound of LFP signals, high gamma, has been hypothesized to include components of firing from nearby neurons, including neurons too distant from the microelectrode to have resolvable waveforms (Ray, 2011) Purpose-built surface micro-electrodes with diameters as small as 10 μm have been used to detect and isolate waveforms of individual action potentials from superficial cortical neurons (Khodagholy, 2015). It is thus likely that the μECoG arrays in this study may record finer, more localized representations of neuronal activity, particularly in the high frequency bands corresponding to spectral peaks of action potential waveforms. This study used spike-triggered averages between single neurons in basal ganglia structures and

cortical μECoG surface recordings to search for patterns of functional connectivity in a high frequency (250-2000 Hz) range matching the peaks in frequency content of individual action potential waveforms, referred to hereafter as the AP band for the sake of brevity. The ability to detect features of action potential spiking using surface electrodes could be particularly useful in clinical applications and research involving human subjects, since penetrating microelectrodes are used much less frequently in these settings due to the inherent tissue damage.

METHODS

Experimental setup and data collection. Eight Parkinsonian patients underwent standard clinical, anesthetized bilateral DBS implant surgery at Barrow Neurological Institute (Phoenix, AZ) (Table 4.1). A burr hole was formed over the dorsal frontal lobe at the entry to the descent tract for the therapeutic DBS electrode. Prior to insertion of the DBS electrode, a 4x4 μECoG array (75 um diameter, 2 mm spacing, PMT Neurosurgical, Chanhassen, MN) (Figure 4.2) was slid epicortically over motor association cortex.

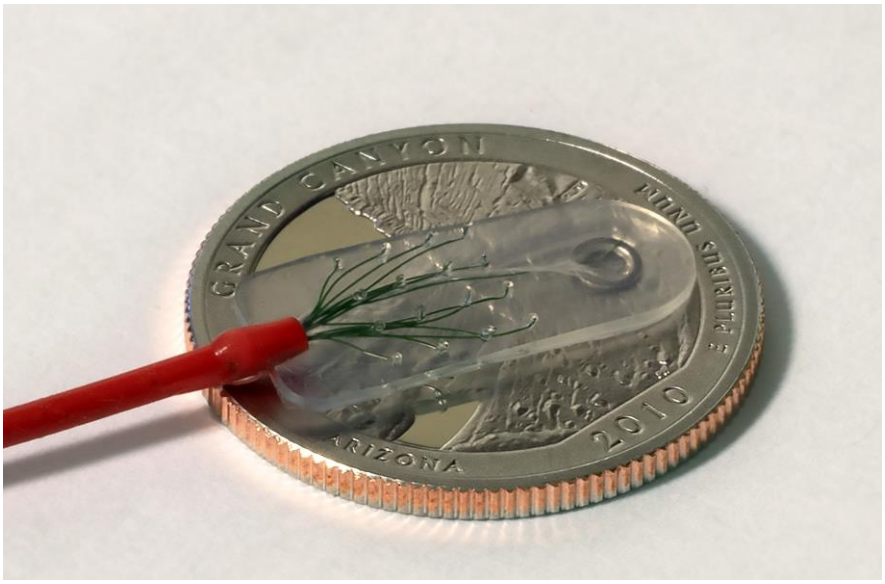

Figure 4.2. PMT surface µECoG. The array used in this study to record cortical local field potentials is shown photographed with a quarter for scale. Electrodes had a 75 µm diameter with 2mm inter-electrode spacing.

A penetrating microelectrode (FHC, Bowdoin, ME) was inserted ipsilaterally through the therapeutic target tracts, pausing at various depths to record neuronal activity including action potentials from subcortical structures, including anterior thalamus, substantia nigra pars reticula, and subthalamic nucleus (tract for STN therapeutic target), or external and internal globus pallidus (tract for GPi therapeutic target). The penetrating microelectrode and the surface µECoG array were then removed, and the therapeutic DBS electrode was inserted along the same tract.

Table 4.1. Patient Demographics

Subject	Age	Sex	Target Structure	Implantation	Years Diagnosed	Recorded Hemisphere
2016PB01	62	M	STN	Bilateral	4	Right
2016PB02	65	M	STN	Bilateral	12	Left
2016PB04	66	F	GPi	Bilateral	10	Right
2016PB05	65	M	STN	Bilateral	6	Right
2016PB06	67	M	STN	Bilateral	6	Right
2017PB01	55	M	STN	Bilateral	7	Right
2017PB02	55	M	GPi	Bilateral	15	Right
2017PB03	62	M	GPi	Bilateral	14	Right

Data from the cortical µECoG array and the subcortical penetrating microelectrode were recorded at 24.4 kHz with a PZ5 data acquisition system (Tucker-Davis Technologies, Alachua, FL). At each pause of the descent, markers for the insertion depth of the penetrating microelectrode and the corresponding basal ganglia structure were manually added to the recording file.

Data analysis. LFP data recorded from the surface µECoG array were downsampled to 4800 Hz for analysis. 60 Hz line noise and harmonics were filtered using 3rd order Butterworth notch filters. The subcortical microelectrode recordings were highpass filtered above 200 Hz to isolate action potential waveforms. Positive and negative voltage spikes beyond 3 times the RMS value of the recording were extracted into 1.6 ms

snippets as candidate action potentials. Candidate snippets were projected into principal component space using the top three principal components. Initial sorting of AP waveforms from neurons at each subcortical recording depth was performed using an automated algorithm based on mixtures of multivariate t-distributions (Shoham, 2003). Cluster grouping and separation was adjusted from the automated process by manual visual inspection of the clusters and their Mahalanobis ellipsoids in PCA space, the interspike interval distributions, spike locations in the voltage time series recording and the collective experience of the researchers conducting the study.

For each isolated subcortical neuron, the spike-triggered average of the surface local field potential was computed for every electrode on the µECoG array from -0.5 to +0.5 seconds relative to subcortical spike times. Electrode 1 was excluded from analysis due to the presence of artifactual contamination from the penetrating microelectrode caused by the recording hardware. Bootstrap resampling of subcortical spike times was performed 500 times at 25% dropout, and a spike-triggered average was generated from each subset of resampled spike times. To generate surrogate baseline data for statistical comparisons, an additional spike-triggered average was generated at each resampling using altered spike times. The alteration of spike times was performed using basic random jitter from 0 - 0.5 seconds in either direction in order to disrupt fine temporal patterns correlated with spike times while preserving slower trends.

For each of the resampled spike-triggered average waveforms, from true and from jittered spike times, instantaneous mean spectral power was computed for six frequency bands. The first five frequency bands are associated with band-limited components of LFP oscillations - Theta (4-7 Hz), Alpha (8-15 Hz), Beta (16 – 30 Hz), Gamma (31-80 Hz),

and Chi (81-160 Hz) - and the sixth frequency band, AP (250-2000 Hz), was chosen for its potential to contain high-frequency features of nearby action potential spikes. To perform this analysis, multi-taper power spectral density estimates were computed from the spike-triggered averages using 0.25 s windows, 80 Hz sampling rates, and a single taper to maximize the frequency resolution. The resulting time-frequency matrices were normalized across frequencies with respect to the average spectrum in order to minimize masking of low amplitude, high frequency signals by higher amplitude, lower frequency signals in each frequency band. Subsets of the resulting normalized time-frequency matrices corresponding to each frequency band were extracted and averaged over frequency bins to create a time-varying index of spike-triggered average spectral power for each frequency band, electrode, and resampling iteration.

For each frequency band, to determine if the spike-triggered average spectral power was different from the surrogate baseline, the resampled spike-triggered average spectral power vectors made from true spike times were projected into Principal Component space along with the STA vectors made from jittered spike times. The first three principal components were used in this projection. Mahalanobis ellipsoids were generated for each STA cluster at 1.96 standard deviations from centroid location, and the two clusters were considered significantly separable if their Mahalanobis ellipsoids did not intersect. Subcortical spike-triggered averages of cortical surface activity that differ significantly from baseline may represent patterns of functional connectivity between individual subcortical neurons and small populations of cortical neurons.

RESULTS

In total, action potential waveforms from 127 neurons were isolated from 73 recording depths across 5 basal ganglia structures in 8 Parkinsonian patients undergoing standard clinical bilateral DBS implant surgery (Table 4.1). The results of the spike sorting process are shown for an example recording depth with 3 neurons in figures 4.3 and 4.4.

Spike-triggered average LFP waveforms showed considerable amplitude reduction compared to raw LFP recordings, dropping from tens or hundreds of μV to single-digit μV amplitudes (Figure 4.5). Modulation in amplitude of activity in various frequency bands, particular Alpha band and the AP band, could be seen both in the spike-triggered average LFP waveforms (Figure 4.5) as well as their corresponding frequency-normalized spectrograms and frequency band-averaged instantaneous spectral power vectors (Figure 4.6).

The increase in high-frequency power observed in spike-triggered average waveforms computed from true spike times went away when spike times were randomly jittered. Results for an example neuron with a large AP band response are shown in Figure 4.7. Significance testing for the difference in activity between resampled spike-triggered averages from true spike times and from jittered spike times was computed via Mahalanobis ellipsoid overlap in PCA space for all neurons, channels, and frequency bands. Results of significance testing for the example neuron with large AP band response are shown in Figure 4.8. Spectrograms of spike-triggered average waveforms are shown for all channels for an example neuron with significant activity in both alpha and AP bands in Figure 4.9, and the corresponding instantaneous mean spectral power for true and jittered

spike-triggered averages is shown for all channels for each frequency band in Figure 4.10. The example data in Figures 4.9 and 4.10 are reflective of the general trends observed in Alpha band and in AP band across patients and basal ganglia structures: increases in cortical alpha band power tended to lead subcortical spike times (mode time difference = -40 ms), while cortical power in AP band tended to lag subcortical spike times (mode time difference = +50 ms) (Figure 4.11). A total of 356 significant spike-triggered average functional couplings were observed between subcortical neurons and activity in AP band from cortical surface electrodes, roughly one order of magnitude more than observed in the next closest frequency range, Alpha band with 34. Table 4.2 summarizes the number of significant functional couplings found by basal ganglia structure and frequency band.

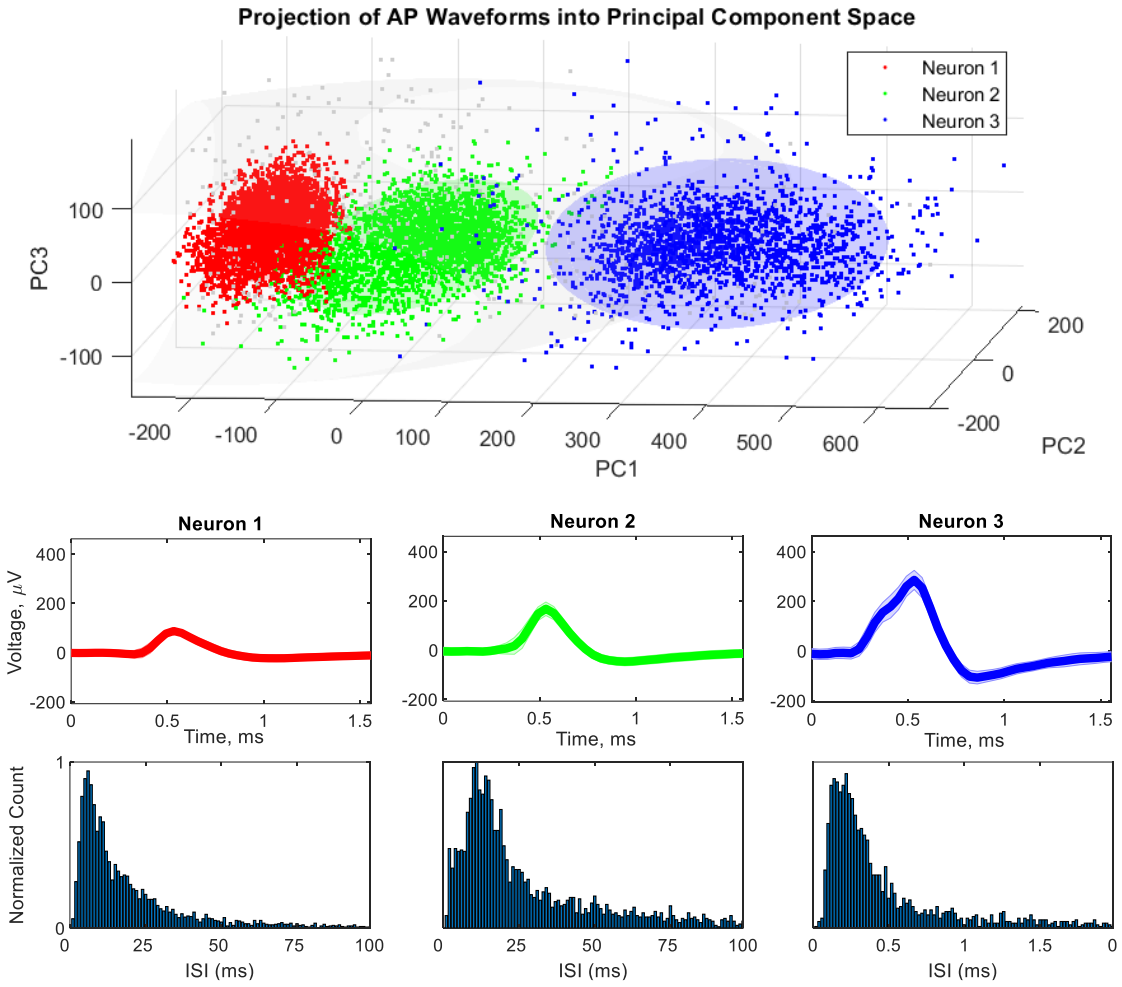

Figure 4.3. AP Waveform Sorting. Top, Principal Component Analysis was performed on all extracted waveform snippets, which were then projected into PCA space using the top 3 principal components. Mahalanobis ellipsoids are superimposed for each cluster to help visualize cluster separation. Cluster grouping and separation was adjusted from an automated process by manual visual inspection of the distribution in PCA space, the interspike interval distributions, spike locations in the voltage time series recording (Figure 4.4). Middle row, mean time series waveforms are shown for each sorted neuron, with shaded area representing ± 1 standard deviation. Bottom row, normalized histogram of inter-spike intervals is shown for each sorted neuron.

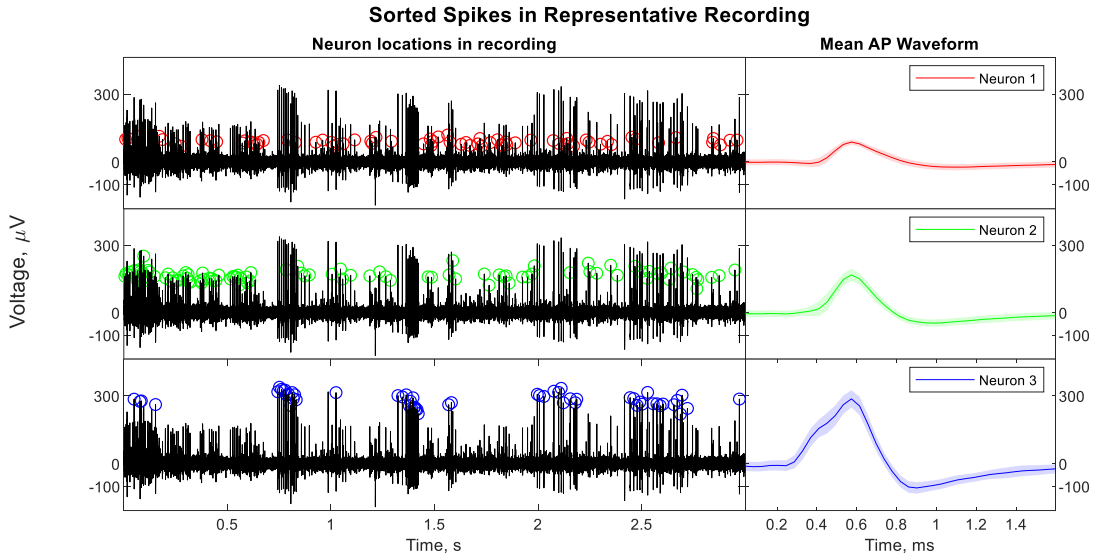

Figure 4.4. Sorted Spikes in Subcortical recording. A representative recording from the subcortical penetrating microelectrode is shown with isolated action potentials from 3 neurons. The same recording segment is shown three times, with spike times highlighted for a different neuron in each plot.

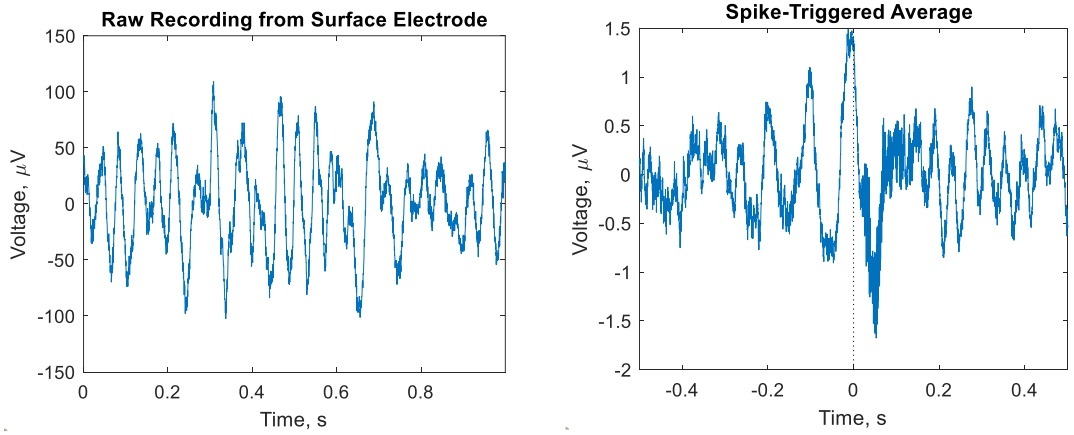

Figure 4.5. Raw Surface LFP and Spike-Triggered Average. Left, a representative 1-second sample recording is shown from an electrode on the surface µECoG array. Right,

the surface potential recorded from the same electrode is shown after averaging from aligning on subcortical action potentials. The dotted black line at t = 0 indicates subcortical spike time. The spike-triggered averaging process reduced signal amplitude in this instance from around 100 µV to around 1 µV, a reduction of 2 orders of magnitude. In the spike-triggered average waveform, prominent alpha band oscillations peak 10-20 ms before spiketime. High frequency activity is also visible from 20-150 ms post spike time.

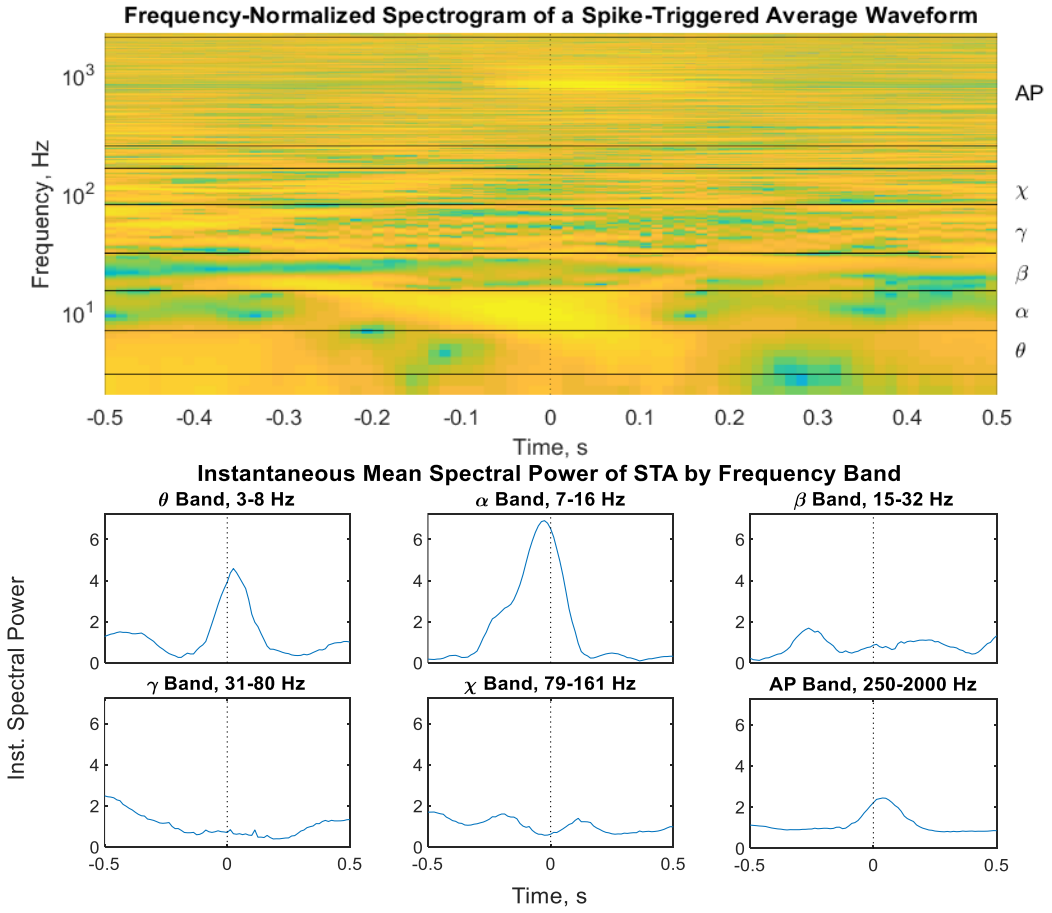

Figure 4.6. STA Spectral Power by Frequency Band. Top, a frequency-normalized spectrogram of the representative spike-triggered average waveform from Figure 4.5 shows the six frequency bands for which instantaneous mean spectral power was

computed. Spike time is indicated by the dotted black line at t = 0, while horizontal solid black lines indicate boundaries of frequency bands. Frequency is plotted on a logarithmic scale to facilitate viewing of all frequency bands together. Increases in spectral power relative to subcortical spike time can be seen in alpha band and the high frequency band potentially associated with action potential spectra, AP band. Bottom, instantaneous mean spectral power is shown for each of the six frequency bands

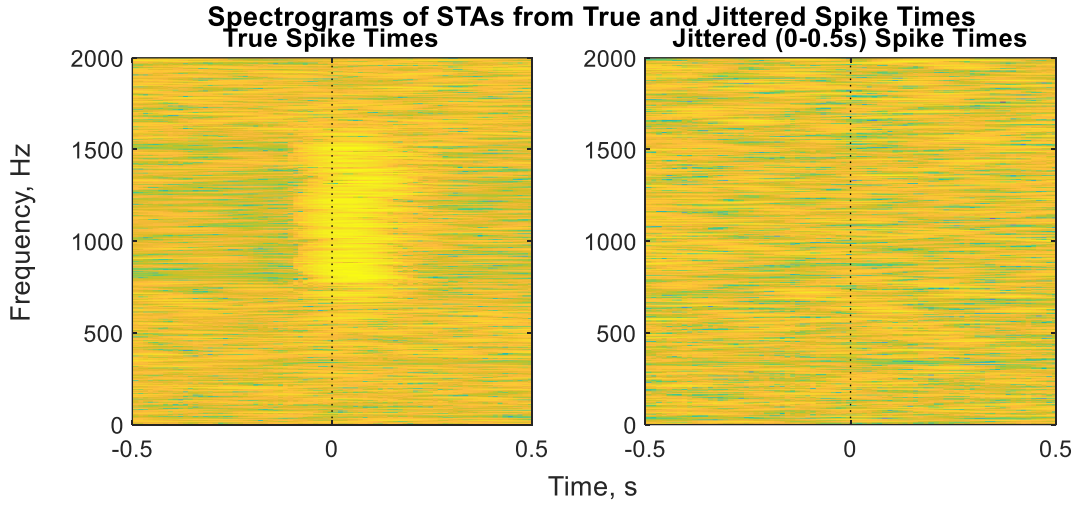

Figure 4.7. Spectrograms of STAs from True and Jittered Spike Times. Data are shown for a representative subcortical neuron with a particularly robust response in AP band in a cortical surface recording. Left, the spectrogram is shown for the STA generated from true spike times. Dotted line at t=0 indicates subcortical spike time. Right, the spectrogram is shown for the STA generated using surrogate spike times, jittered randomly from 0.5s in either direction from true spike times. The increase in high frequency power relative to spike time is not present the STA generated from jittered spike times. Instantaneous mean spectral power in AP band and significance testing shown in Figure 4.8.

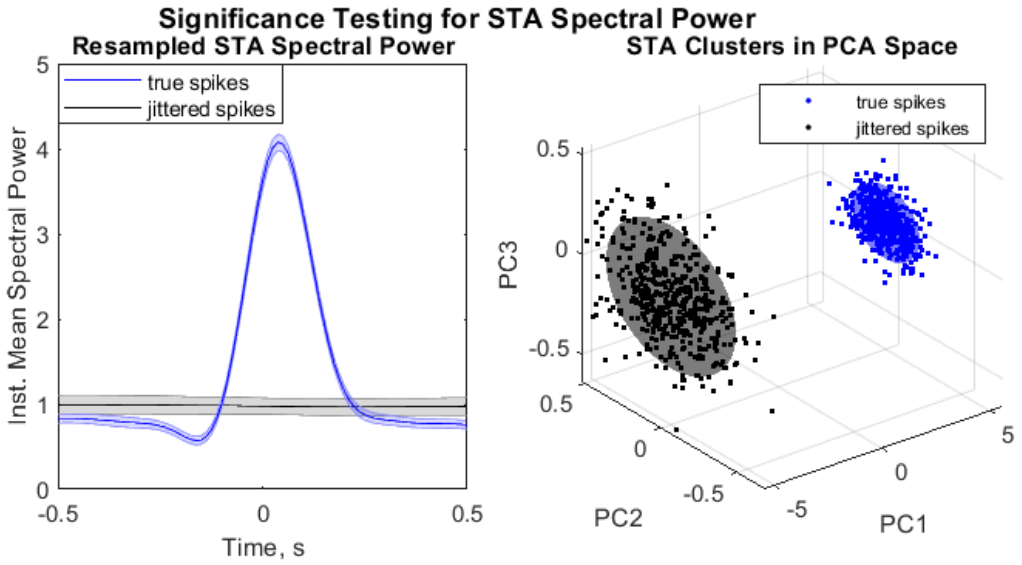

Figure 4.8. Significance Testing for STA Spectral Power for a Representative Neuron. The data are computed from the same channel recording as the spectrograms shown in Figure 4.7. Left, the mean waveforms of resampled STA spectral power in AP band are shown for true spike times (blue) and for surrogate spike times, jittered randomly from 0.5s in either direction from true spike times (black). Shaded areas are ± 1.96 standard deviations of the resampled vectors from the mean. Right, the resampled STA spectral power vectors are projected into Principal Component Space using the first 3 principal components. Mahalanobis Ellipsoids are shown at 1.96 standard deviations for the clusters in PCA space from STAs made from true spike times (blue) and from jittered spike times (black). The STA spectral power from true spike times was classified as significantly different from baseline as the ellipsoids do not intersect.

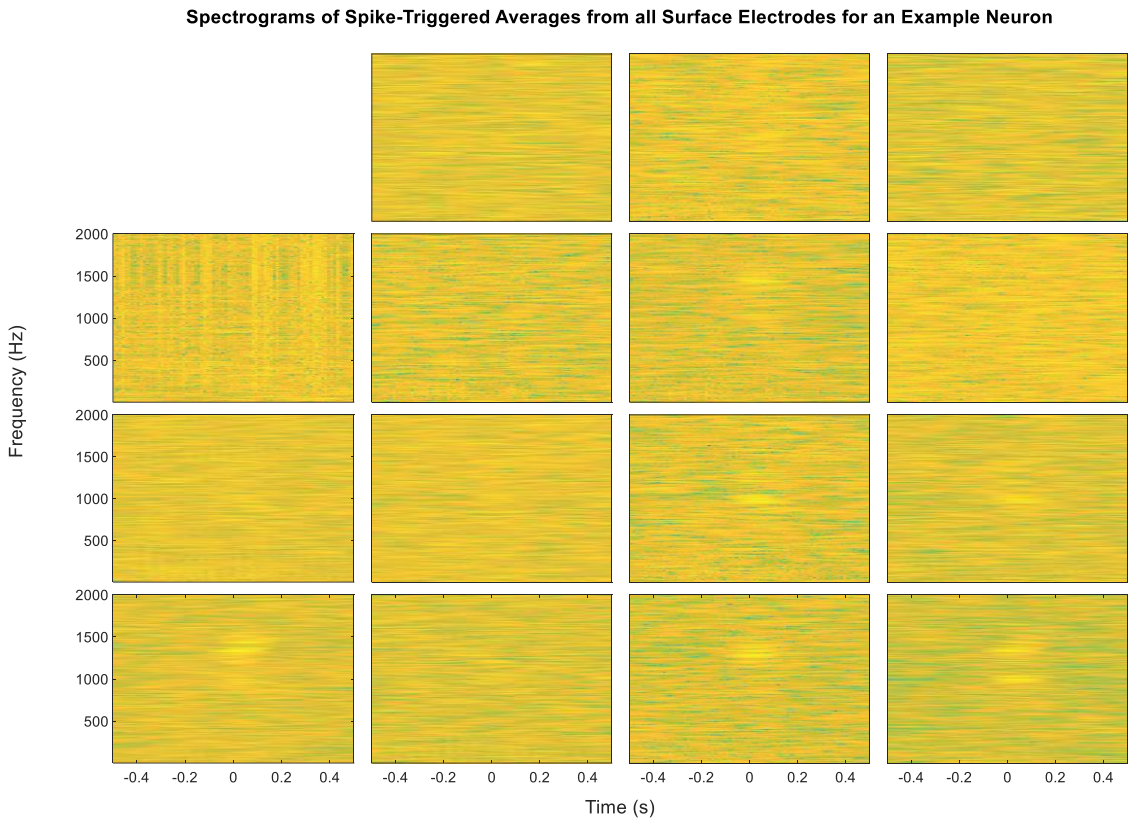

Figure 4.9. Frequency-Normalized Spectrograms of STA LFP. Time-frequency plots from surface recordings are shown relative to subcortical spike times for an example neuron in STN. Subplots correspond to physical location of electrodes on the surface µECoG array. Electrode 1 (upper left) was excluded from analysis due to recording artifacts. Several channels show increases in power in localized bands ranging from 800 – 1600 Hz approximately centered on subcortical spike time, including all electrodes in the third column. Frequency is plotted on a linear scale to facilitate viewing of activity in AP band. Instantaneous mean spectral power and significance by frequency band and channel are shown below in Figure 4.10.

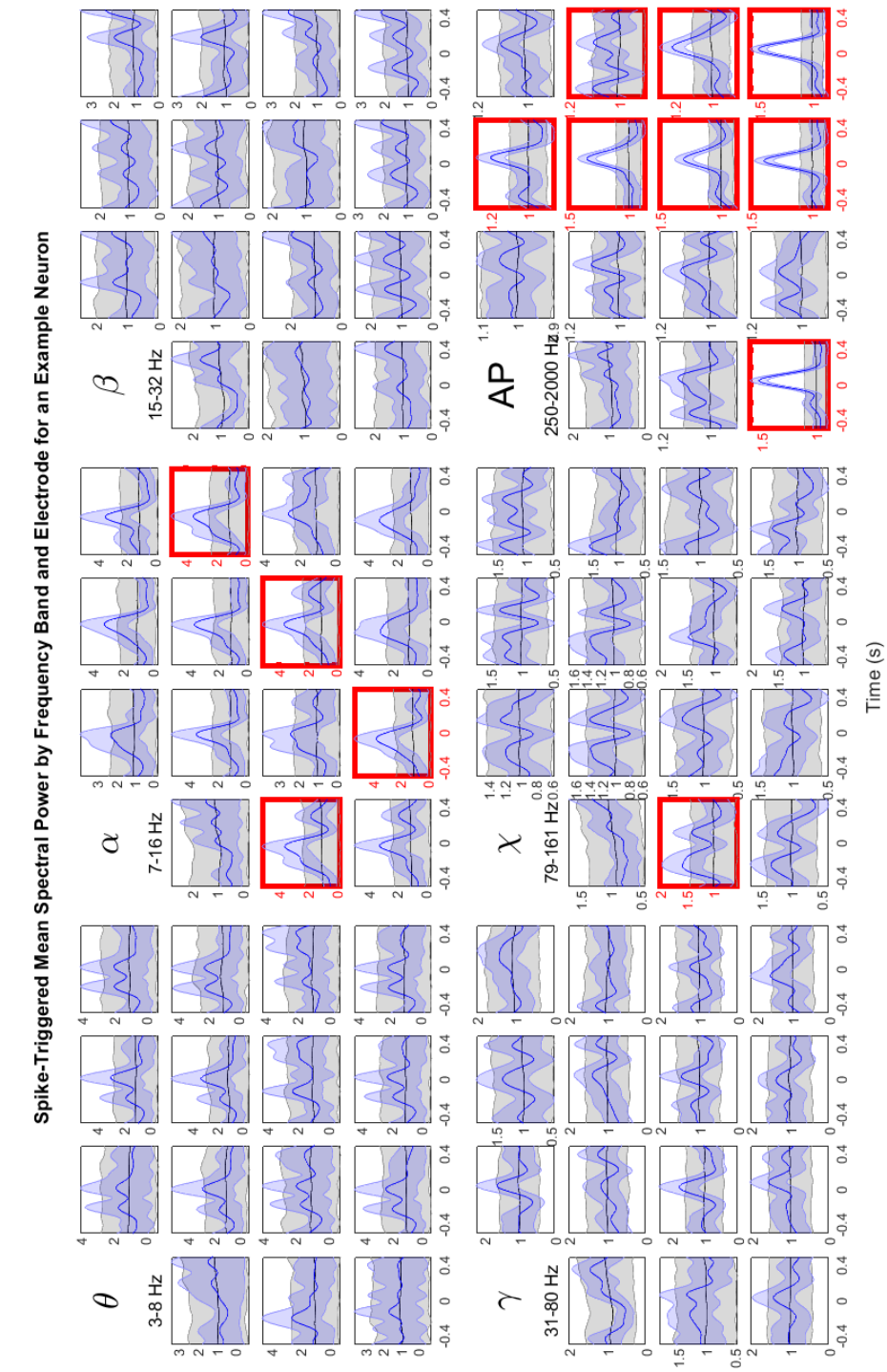
Spike-Triggered Mean Spectral Power by Frequency Band and Electrode for an Example Neuron
θ
3-8 Hz
α
7-16 Hz
β
15-32 Hz
γ
31-80 Hz
χ
79-161 Hz
AP
250-2000 Hz
Time (s)
Instantaneous STA Power in Frequency Band

Figure 4.10. Significantly Coupled STA Spectral Power Means. Data are shown for an example subcortical neuron in STN. Increases in power roughly centered on subcortical spike time can be seen in cortical surface recordings in Alpha band and the very high frequency band. Subplots for each frequency band correspond to physical location of electrodes on the surface μECoG array. Blue time series plots represent mean spectral power for spike-triggered averages resampled from true spike times, while black plots represent mean spectral power averaged and resampled from surrogate, jittered spike times. Shaded areas are ± 1.96 standard deviations of the resampled vectors from the mean. Red bolded subplots indicate mean STA spectral power vectors that were significantly different from the surrogate baseline vector, i.e. resampled distributions whose clusters in PCA space did not overlap at 2 Mahalanobis standard deviations.

Table 4.2. Summary of Significant Functional Couplings. The top section tabulates by Basal Ganglia structure the total number of recorded depths and isolated neurons, and again for the recordings and neurons that had any significant functional couplings between subcortical spikes and cortical surface recordings for at least one neuron, in at least one frequency band, on at least one channel. The bottom section shows the summary by

frequency band for the neurons with significant functional coupling on at least one channel in at least one frequency band.

	AT	STN	SNr	GPe	GPi	Total
Total subcortical recording depths	3	32	5	15	18	73
Total recorded neurons (Table 4.1)	7	54	14	19	33	127
Subcortical recordings correlated with cortical LFP	2	29	4	6	14	55
Neurons correlated with cortical LFP	3	42	10	7	21	83
Significantly coupled neurons by frequency: Theta	0	9	2	1	0	12
Alpha	0	10	0	0	1	11
Beta	0	1	1	1	2	5
Gamma	0	2	0	1	3	6
Chi	1	14	1	2	1	19
AP Band	1	25	3	4	9	42

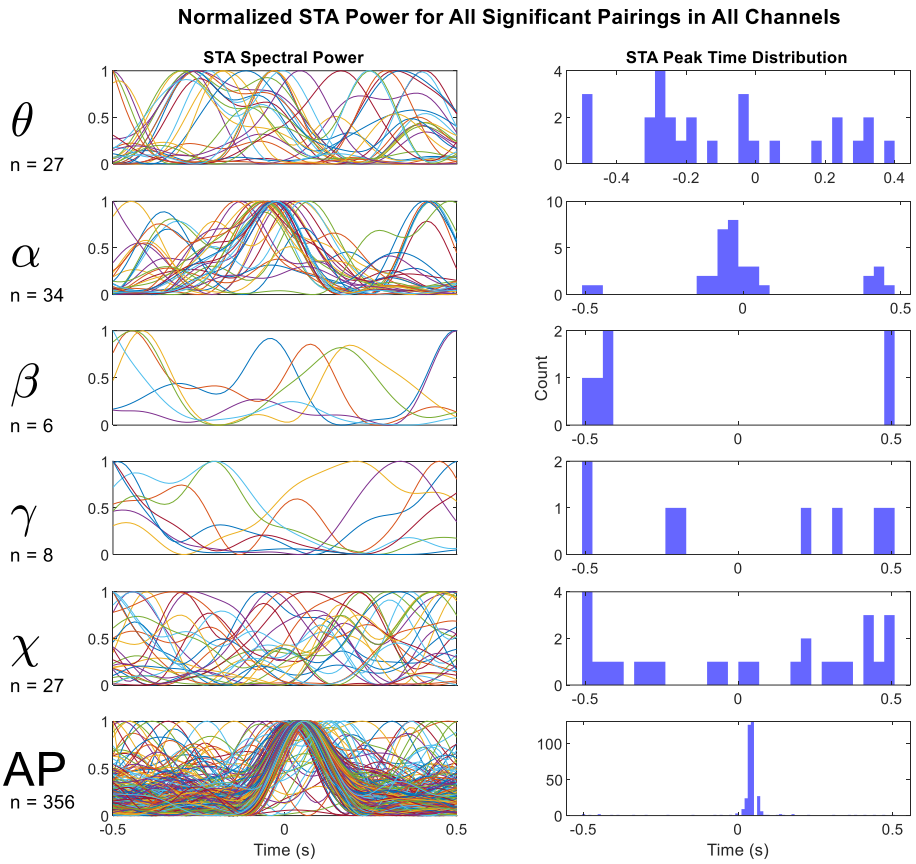

Figure 4.11. Normalized STA Power for All Significant Pairings in all Channels. Across all patients and Basal Ganglia structures, the AP band (250-2000 Hz) showed significant coupling in 356 pairs of subcortical neuron to cortical surface recordings, out of 1,905 total pairs per frequency band. Alpha band showed the next greatest amount, at 34 significantly coupled pairs. Increases in STA spectral power had modes of -270 ms relative to subcortical spike time in Theta band, -40 ms in Alpha Band, and +50 ms in AP Band. Distributions of spectral power increase in Beta, Gamma and Chi bands did not show a clear central tendency.

DISCUSSION

356 significant spike-triggered trends were observed among all subcortical neuron to surface electrode pairs in the AP band, out of 1,905 total pairs, or 19%. This is an order of magnitude higher than the number of significant trends observed in any other frequency band. This discrepancy might be related to fundamental differences between the nature of action potential spiking and the bandlimited synchronous oscillations in LFP signals, and the amplitude reduction induced by the spike-triggered averaging process. LFP waveforms averaged by alignment on spike times inherently undergo large amounts of destructive interference from averaging out-of-phase snippets together, driving the averaged amplitude towards 0. STA waveforms in this study showed amplitudes 2 orders of magnitude lower than raw LFP signals. Similar amplitude reduction has been observed in STA waveforms recorded from penetrating microelectrodes in macaques, and the reduction was noted to increase with increasing LFP frequency and greater distance between electrodes (Ray 2011). Phase locking of action potentials to a certain frequency band of the LFP signal results in attenuation of the destructive interference as the spike-centered snippets are overall more synchronous, resulting in greater amplitude of the average waveform in that frequency band relative to spike time. Spike-triggered trends in LFP frequency bands thus reflect patterns in signal phase relative to spike time, and not just patterns in amplitude of the signal in the frequency band.

Action potentials, however, are orders of magnitude shorter-lived than LFP oscillations (commonly sub-ms for single AP waveforms, vs an approximately 100 ms period for 1 oscillation of Alpha band) and are effectively only one “cycle” long, as

opposed to the continuous oscillations of LFP signals. Signal interference of individual action potential waveforms, destructive or constructive, would require correspondingly tighter temporal alignment of individual spike-centered snippets in order to occur. Additionally, action potential waveforms often exhibit a much larger positive than negative phase (or vice versa, depending on factors such as electrode orientation relative to the cell body) (Buzsaki, 2012), which could limit the amount of destructive interference even upon exact temporal alignment of positive and negative phases. It is therefore possible that spike-triggered average waveforms could be less affected by synchrony of continuous oscillations in the very high (250-2000 Hz) frequency range compared to the sensitivity of STA waveforms to synchrony of continuous oscillations in other, lower frequency bands. Rather than reflecting synchrony of oscillations between 250-2000 Hz, spike-triggered trends in the presumed AP band could reflect the total amount of spiking from the local neuronal population, or gross local firing rate.

Surprisingly, almost no significant trends were observed in Beta band between subcortical neurons and surface field potentials, despite aberrant coupling in beta band being a hallmark of Parkinsonian pathology. One possible explanation could be that anesthesia has been noted to have pronounced effects on brain activity (Rojas, 2006; Potez, 2008). Anesthesia has been noted to have several particular effects on functional connectivity in different subcortical and cortical regions. Propofol has been observed in BOLD fMRI studies to reduce functional connectivity between thalamus and cortex, (Liu, 2013), while sevoflurane has been seen to reduce significant voxels in functional connectivity maps by up to 98% in deep anesthesia (Peltier 2005). Biophysical models of neuronal dynamics have indicated that beta oscillations can be generated by the effect of

propofol in cortex alone, without necessarily requiring thalamic participation (McCarthy 2008). Anesthesia has been associated with wider synchronization in the brain, particularly in low-frequency rhythms, which have been linked to layer specific pyramidal neurons acting as local pacemakers (Bollimunta, 2008).

The spectrograms of cortical surface STAs show frequency localization of the increase in AP band activity; rather than a broadband increase tapering off from lower frequency bands such as gamma or chi, distinct peaks were typically observed between 800-1600 Hz. Additionally, increases in cortical AP band activity showed tight temporal coupling relative to subcortical spike times, with a mode lag time of 50 ms across patients and basal ganglia structures, with less variance than observed in lower frequency bands. One possible explanation for the low variance and consistently short lag from subcortical spike to cortical peak in AP band power is that propagation time of axons, synaptic neurotransmitter diffusion, and reciprocally coupled neuron recursion time have been observed to be on the order of 10 ms or less (Shepherd 2004; Sabatini 1996; Koch 2004; Ray 2008). While far from definitive, the frequency localization and tight temporal coupling of the 250-2000 Hz frequency band are consistent with a possible contribution of action potential waveforms in a local population recorded from the surface electrodes. Rather than representing spike-field coupling, significant coupling in the high frequency band from 250-2000 Hz could instead possibly represent a form of rapid spike-to-spike coupling.

REFERENCES

Albin, R. L., Young, A. B., & Penney, J. B. (1989). The functional anatomy of basal ganglia disorders. *Trends in Neurosciences, 12*(10), 366-375.

Baker, J., Bishop, W., Kellis, S., Levy, T., House, P., & Greger, B. (2009). Multi-scale recordings for neuroprosthetic control of finger movements. *Conference Proceedings: ...Annual International Conference of the IEEE Engineering in Medicine and Biology Society.IEEE Engineering in Medicine and Biology Society.Annual Conference, 2009*, 4573-4577.

Barrese, J. C., Rao, N., Paroo, K., Triebwasser, C., Vargas-Irwin, C., Franquemont, L., et al. (2013). Failure mode analysis of silicon-based intracortical microelectrode arrays in non-human primates. *Journal of Neural Engineering, 10*(6), 066014-2560/10/6/066014. Epub 2013 Nov 12.

Bedard, C., Kroger, H., & Destexhe, A. (2004). Modeling extracellular field potentials and the frequency-filtering properties of extracellular space. *Biophysical Journal, 86*(3), 1829-1842.

Besson, P., Andermann, F., Dubeau, F., & Bernasconi, A. (2008). Small focal cortical dysplasia lesions are located at the bottom of a deep sulcus. *Brain : A Journal of Neurology, 131*(Pt 12), 3246-3255.

Biran, R., Martin, D. C., & Tresco, P. A. (2005). Neuronal cell loss accompanies the brain tissue response to chronically implanted silicon microelectrode arrays. *Experimental Neurology, 195*(1), 115-126.

Bollimunta, A., Chen, Y., Schroeder, C. E., & Ding, M. (2008). Neuronal mechanisms of cortical alpha oscillations in awake-behaving macaques. *The Journal of Neuroscience : The Official Journal of the Society for Neuroscience, 28*(40), 9976-9988.

Brown, P. (2007). Abnormal oscillatory synchronisation in the motor system leads to impaired movement. *Current Opinion in Neurobiology, 17*(6), 656-664.

BuzsÃ¡ki, G., Anastassiou, C. A., & Koch, C. (2012). The origin of extracellular fields and currents â€" EEG, ECoG, LFP and spikes. *Nature Reviews. Neuroscience, 13*(6), 407-420.

Chao, Z. C., Nagasaka, Y., & Fujii, N. (2010). Long-term asynchronous decoding of arm motion using electrocorticographic signals in monkeys. *Frontiers in Neuroengineering, 3*, 3.

Chestek, C. A., Gilja, V., Nuyujukian, P., Foster, J. D., Fan, J. M., Kaufman, M. T., et al. (2011). Long-term stability of neural prosthetic control signals from silicon cortical arrays in rhesus macaque motor cortex. *Journal of Neural Engineering, 8*(4), 045005-2560/8/4/045005. Epub 2011 Jul 20.

Christie, B. P., Ashmont, K. R., House, P. A., & Greger, B. (2016). Approaches to a cortical vision prosthesis: Implications of electrode size and placement. *Journal of Neural Engineering, 13*(2), 025003-2560/13/2/025003. Epub 2016 Feb 23.

Cimenser, A., Purdon, P. L., Pierce, E. T., Walsh, J. L., Salazar-Gomez, A. F., Harrell, P. G., et al. (2011). Tracking brain states under general anesthesia by using global coherence analysis. *Proceedings of the National Academy of Sciences, 108*(21), 8832-8837. doi:10.1073/pnas.1017041108

Clower, D. M., Dum, R. P., & Strick, P. L. (2005). Basal ganglia and cerebellar inputs to 'AIP'. *Cerebral Cortex (New York, N.Y.: 1991), 15*(7), 913-920.

de Hemptinne, C., Ryapolova-Webb, E. S., Air, E. L., Garcia, P. A., Miller, K. J., Ojemann, J. G., et al. (2013). Exaggerated phase-amplitude coupling in the primary motor cortex in parkinson disease. *Proceedings of the National Academy of Sciences of the United States of America, 110*(12), 4780-4785.

de Hemptinne, C., Swann, N. C., Ostrem, J. L., Ryapolova-Webb, E. S., San Luciano, M., Galifianakis, N. B., et al. (2015). Therapeutic deep brain stimulation reduces cortical phase-amplitude coupling in parkinson's disease. *Nature Neuroscience, 18*(5), 779-786.

Degenhart, A. D., Eles, J., Dum, R., Mischel, J. L., Smalianchuk, I., Endler, B., et al. (2016). Histological evaluation of a chronically-implanted electrocorticographic electrode grid in a non-human primate. *Journal of Neural Engineering, 13*(4), 046019-2560/13/4/046019. Epub 2016 Jun 28.

DeLong, M. R. (1990). Primate models of movement disorders of basal ganglia origin. *Trends in Neurosciences, 13*(7), 281-285.

Egan, J., Baker, J., House, P. A., & Greger, B. (2012). Decoding dexterous finger movements in a neural prosthesis model approaching real-world conditions. *IEEE*

Transactions on Neural Systems and Rehabilitation Engineering : A Publication of the IEEE Engineering in Medicine and Biology Society, *20*(6), 836-844.

Flint, R. D., Lindberg, E. W., Jordan, L. R., Miller, L. E., & Slutzky, M. W. (2012). Accurate decoding of reaching movements from field potentials in the absence of spikes. *Journal of Neural Engineering*, *9*(4), 046006-2560/9/4/046006. Epub 2012 Jun 25.

Flores, F. J., Hartnack, K. E., Fath, A. B., Kim, S. E., Wilson, M. A., Brown, E. N., et al. (2017). Thalamocortical synchronization during induction and emergence from propofol-induced unconsciousness. *Proceedings of the National Academy of Sciences of the United States of America*, *114*(32), E6660-E6668.

Friedman, E. B., Sun, Y., Moore, J. T., Hung, H. T., Meng, Q. C., Perera, P., et al. (2010). A conserved behavioral state barrier impedes transitions between anesthetic-induced unconsciousness and wakefulness: Evidence for neural inertia. *PloS One*, *5*(7), e11903.

Fukushima, M., Saunders, R. C., Mullarkey, M., Doyle, A. M., Mishkin, M., & Fujii, N. (2014). An electrocorticographic electrode array for simultaneous recording from medial, lateral, and intrasulcal surface of the cortex in macaque monkeys. *Journal of Neuroscience Methods*, *233*, 155-165.

Hackett, T. A. (2011). Information flow in the auditory cortical network. *Hearing Research*, *271*(1-2), 133-146.

Hanrahan, S. J., Greger, B., Parker, R. A., Ogura, T., Obara, S., Egan, T. D., et al. (2013). The effects of propofol on local field potential spectra, action potential firing rate, and their temporal relationship in humans and felines. *Frontiers in Human Neuroscience*, *7*, 136.

Henle, C., Raab, M., Cordeiro, J. G., Doostkam, S., Schulze-Bonhage, A., Stieglitz, T., et al. (2011). First long term in vivo study on subdurally implanted micro-ECoG electrodes, manufactured with a novel laser technology. *Biomedical Microdevices*, *13*(1), 59-68.

Hoover, J. E., & Strick, P. L. (1999). The organization of cerebellar and basal ganglia outputs to primary motor cortex as revealed by retrograde transneuronal transport of herpes simplex virus type 1. *The Journal of Neuroscience : The Official Journal of the Society for Neuroscience*, *19*(4), 1446-1463.

Jin, J. Z., Weng, C., Yeh, C. I., Gordon, J. A., Ruthazer, E. S., Stryker, M. P., et al. (2008). On and off domains of geniculate afferents in cat primary visual cortex. *Nature Neuroscience, 11*(1), 88-94.

Jorfi, M., Skousen, J. L., Weder, C., & Capadona, J. R. (2015). Progress towards biocompatible intracortical microelectrodes for neural interfacing applications. *Journal of Neural Engineering, 12*(1), 011001-2560/12/1/011001. Epub 2014 Dec 2.

Katzner, S., Nauhaus, I., Benucci, A., Bonin, V., Ringach, D. L., & Carandini, M. (2009). Local origin of field potentials in visual cortex. *Neuron, 61*(1), 35-41.

Kellis, S., Greger, B., Hanrahan, S., House, P., & Brown, R. (2011). Platinum microwire for subdural electrocorticography over human neocortex: Millimeter-scale spatiotemporal dynamics. *Conference Proceedings : ...Annual International Conference of the IEEE Engineering in Medicine and Biology Society.IEEE Engineering in Medicine and Biology Society.Annual Conference, 2011*, 4761-4765.

Kellis, S., Miller, K., Thomson, K., Brown, R., House, P., & Greger, B. (2010). Decoding spoken words using local field potentials recorded from the cortical surface. *Journal of Neural Engineering, 7*(5), 056007-2560/7/5/056007. Epub 2010 Sep 1.

Kellis, S., Sorensen, L., Darvas, F., Sayres, C., O'Neill, K.,3rd, Brown, R. B., et al. (2016). Multi-scale analysis of neural activity in humans: Implications for micro-scale electrocorticography. *Clinical Neurophysiology : Official Journal of the International Federation of Clinical Neurophysiology, 127*(1), 591-601.

Khodagholy, D., Gelinas, J. N., Thesen, T., Doyle, W., Devinsky, O., Malliaras, G. G., et al. (2015). NeuroGrid: Recording action potentials from the surface of the brain. *Nature Neuroscience, 18*(2), 310-315.

Koch C (2004) Biophysics of Computation: Information Processing in Single Neurons (Computational Neuroscience Series). New York, NY, USA: Oxford University Press, Inc.

Lacour, S. P., Benmerah, S., Tarte, E., FitzGerald, J., Serra, J., McMahon, S., et al. (2010). Flexible and stretchable micro-electrodes for in vitro and in vivo neural interfaces. *Medical & Biological Engineering & Computing, 48*(10), 945-954.

Lalo, E., Thobois, S., Sharott, A., Polo, G., Mertens, P., Pogosyan, A., et al. (2008). Patterns of bidirectional communication between cortex and basal ganglia during

movement in patients with parkinson disease. *The Journal of Neuroscience : The Official Journal of the Society for Neuroscience, 28*(12), 3008-3016.

Lanciego, J. L., Luquin, N., & Obeso, J. A. (2012). Functional neuroanatomy of the basal ganglia. *Cold Spring Harbor Perspectives in Medicine, 2*(12), a009621.

Lawrence, S. M., Larsen, J. O., Horch, K. W., Riso, R., & Sinkjaer, T. (2002). Long-term biocompatibility of implanted polymer-based intrafascicular electrodes. *Journal of Biomedical Materials Research, 63*(5), 501-506.

Leski, S., Linden, H., Tetzlaff, T., Pettersen, K. H., & Einevoll, G. T. (2013). Frequency dependence of signal power and spatial reach of the local field potential. *PLoS Computational Biology, 9*(7), e1003137.

Lewis, L. D., Piantoni, G., Peterfreund, R. A., Eskandar, E. N., Harrell, P. G., Akeju, O., et al. (2018). A transient cortical state with sleep-like sensory responses precedes emergence from general anesthesia in humans. *Elife, 7*, 10.7554/eLife.33250.

Lewis, L. D., Weiner, V. S., Mukamel, E. A., Donoghue, J. A., Eskandar, E. N., Madsen, J. R., et al. (2012). Rapid fragmentation of neuronal networks at the onset of propofol-induced unconsciousness. *Proceedings of the National Academy of Sciences of the United States of America, 109*(49), E3377-86.

Liu, X., Lauer, K. K., Ward, B. D., Li, S. J., & Hudetz, A. G. (2013). Differential effects of deep sedation with propofol on the specific and nonspecific thalamocortical systems: A functional magnetic resonance imaging study.*Anesthesiology, 118*(1), 59-69.

Logothetis, N. K., Kayser, C., & Oeltermann, A. (2007). In vivo measurement of cortical impedance spectrum in monkeys: Implications for signal propagation. *Neuron, 55*(5), 809-823.

Lopez-Azcarate, J., Tainta, M., Rodriguez-Oroz, M. C., Valencia, M., Gonzalez, R., Guridi, J., et al. (2010). Coupling between beta and high-frequency activity in the human subthalamic nucleus may be a pathophysiological mechanism in parkinson's disease. *The Journal of Neuroscience : The Official Journal of the Society for Neuroscience, 30*(19), 6667-6677.

Manning, J. R., Jacobs, J., Fried, I., & Kahana, M. J. (2009). Broadband shifts in local field potential power spectra are correlated with single-neuron spiking in humans. *The*

Journal of Neuroscience : The Official Journal of the Society for Neuroscience, 29(43), 13613-13620.

Matsuo, T., Kawasaki, K., Osada, T., Sawahata, H., Suzuki, T., Shibata, M., et al. (2011). Intrasulcal electrocorticography in macaque monkeys with minimally invasive neurosurgical protocols. *Frontiers in Systems Neuroscience, 5*, 34.

McCarthy, M. M., Brown, E. N., & Kopell, N. (2008). Potential network mechanisms mediating electroencephalographic beta rhythm changes during propofol-induced paradoxical excitation. *The Journal of Neuroscience : The Official Journal of the Society for Neuroscience, 28*(50), 13488-13504.

Miller, K. J., Honey, C. J., Hermes, D., Rao, R. P., denNijs, M., & Ojemann, J. G. (2014). Broadband changes in the cortical surface potential track activation of functionally diverse neuronal populations. *Neuroimage, 85 Pt 2*, 711-720.

Miller, K. J., Sorensen, L. B., Ojemann, J. G., & den Nijs, M. (2009). Power-law scaling in the brain surface electric potential. *PLoS Computational Biology, 5*(12), e1000609.

Miller, K. J., Zanos, S., Fetz, E. E., den Nijs, M., & Ojemann, J. G. (2009). Decoupling the cortical power spectrum reveals real-time representation of individual finger movements in humans. *The Journal of Neuroscience : The Official Journal of the Society for Neuroscience, 29*(10), 3132-3137.

Mink, J. W. (2003). The basal ganglia and involuntary movements: Impaired inhibition of competing motor patterns. *Archives of Neurology, 60*(10), 1365-1368.

Mink, J. W., & Thach, W. T. (1993). Basal ganglia intrinsic circuits and their role in behavior. *Current Opinion in Neurobiology, 3*(6), 950-957.

Mountcastle, V. B. (1997). The columnar organization of the neocortex. *Brain : A Journal of Neurology, 120 (Pt 4)*(Pt 4), 701-722.

Nauhaus, I., Busse, L., Carandini, M., & Ringach, D. L. (2009). Stimulus contrast modulates functional connectivity in visual cortex. *Nature Neuroscience, 12*(1), 70-76.

Obeso, J. A., Rodriguez-Oroz, M. C., Rodriguez, M., Lanciego, J. L., Artieda, J., Gonzalo, N., et al. (2000). Pathophysiology of the basal ganglia in parkinson's disease. *Trends in Neurosciences, 23*(10 Suppl), S8-19.

Oswalt, D., Zhou, D., Tobey, D., Datta, P., Talbot, N., Greenberg, R., . . . Greger, B. (2016). The potential for evoking visual perception using epicortical microelectrodes: micro-stimulation of primary visual cortex in the nonhuman primate. Paper presented at the Society for Neuroscience, San Diego.

Peltier, S. J., Kerssens, C., Hamann, S. B., Sebel, P. S., Byas-Smith, M., & Hu, X. (2005). Functional connectivity changes with concentration of sevoflurane anesthesia. *Neuroreport, 16*(3), 285-288.

Perge, J. A., Zhang, S., Malik, W. Q., Homer, M. L., Cash, S., Friehs, G., et al. (2014). Reliability of directional information in unsorted spikes and local field potentials recorded in human motor cortex. *Journal of Neural Engineering, 11*(4), 046007-2560/11/4/046007. Epub 2014 Jun 12.

Polikov, V. S., Tresco, P. A., & Reichert, W. M. (2005). Response of brain tissue to chronically implanted neural electrodes. *Journal of Neuroscience Methods, 148*(1), 1-18.

Potez, S., & Larkum, M. E. (2008). Effect of common anesthetics on dendritic properties in layer 5 neocortical pyramidal neurons. *Journal of Neurophysiology, 99*(3), 1394-1407.

Ray, S., & Maunsell, J. H. (2011). Different origins of gamma rhythm and high-gamma activity in macaque visual cortex. *PLoS Biology, 9*(4), e1000610.

Ray, S., & Maunsell, J. H. (2011). Network rhythms influence the relationship between spike-triggered local field potential and functional connectivity. *The Journal of Neuroscience : The Official Journal of the Society for Neuroscience, 31*(35), 12674-12682.

Ray, S., Crone, N. E., Niebur, E., Franaszczuk, P. J., & Hsiao, S. S. (2008). Neural correlates of high-gamma oscillations (60–200 hz) in macaque local field potentials and their potential implications in electrocorticography. *The Journal of Neuroscience, 28*(45), 11526-11536. doi:10.1523/JNEUROSCI.2848-08.2008

Ribas, G. C. (2010). The cerebral sulci and gyri. *Neurosurgical Focus, 28*(2), E2.

Rojas, M. J., Navas, J. A., & Rector, D. M. (2006). Evoked response potential markers for anesthetic and behavioral states. *American Journal of Physiology.Regulatory, Integrative and Comparative Physiology, 291*(1), R189-96.

Ryu, S. I., & Shenoy, K. V. (2009). Human cortical prostheses: Lost in translation? *Neurosurgical Focus, 27*(1), E5.

Sabatini, B. L., & Regehr, W. G. (1996). Timing of neurotransmission at fast synapses in the mammalian brain. *Nature, 384*(6605), 170-172.

Schendel, A. A., Nonte, M. W., Vokoun, C., Richner, T. J., Brodnick, S. K., Atry, F., et al. (2014). The effect of micro-ECoG substrate footprint on the meningeal tissue response. *Journal of Neural Engineering, 11*(4), 046011-2560/11/4/046011. Epub 2014 Jun 18.

Schendel, A. A., Thongpang, S., Brodnick, S. K., Richner, T. J., Lindevig, B. D., Krugner-Higby, L., et al. (2013). A cranial window imaging method for monitoring vascular growth around chronically implanted micro-ECoG devices. *Journal of Neuroscience Methods, 218*(1), 121-130.

Schwartz, A. B., Cui, X. T., Weber, D. J., & Moran, D. W. (2006). Brain-controlled interfaces: Movement restoration with neural prosthetics. *Neuron, 52*(1), 205-220.

Sellers, K. K., Bennett, D. V., Hutt, A., & Frohlich, F. (2013). Anesthesia differentially modulates spontaneous network dynamics by cortical area and layer. *Journal of Neurophysiology, 110*(12), 2739-2751.

Shepherd GM (2004) The synaptic organization of the brain. OxfordNew York: Oxford University Press. pp xiv, 719.

Shimamoto, S. A., Ryapolova-Webb, E. S., Ostrem, J. L., Galifianakis, N. B., Miller, K. J., & Starr, P. A. (2013). Subthalamic nucleus neurons are synchronized to primary motor cortex local field potentials in parkinson's disease. *The Journal of Neuroscience : The Official Journal of the Society for Neuroscience, 33*(17), 7220-7233.

Shoham, S., Fellows, M. R., & Normann, R. A. (2003). Robust, automatic spike sorting using mixtures of multivariate t-distributions. *Journal of Neuroscience Methods, 127*(2), 111-122.

Terao, Y., Ugawa, Y., Yamamoto, T., Sakurai, Y., Masumoto, T., Abe, O., et al. (2007). Primary face motor area as the motor representation of articulation. *Journal of Neurology, 254*(4), 442-447.

Viventi, J., Kim, D. H., Vigeland, L., Frechette, E. S., Blanco, J. A., Kim, Y. S., et al. (2011). Flexible, foldable, actively multiplexed, high-density electrode array for mapping brain activity in vivo. *Nature Neuroscience, 14*(12), 1599-1605.

Wang, D., Zhang, Q., Li, Y., Wang, Y., Zhu, J., Zhang, S., et al. (2014). Long-term decoding stability of local field potentials from silicon arrays in primate motor cortex during a 2D center out task. *Journal of Neural Engineering, 11*(3), 036009-2560/11/3/036009. Epub 2014 May 8.

Xing, D., Yeh, C. I., & Shapley, R. M. (2009). Spatial spread of the local field potential and its laminar variation in visual cortex. *The Journal of Neuroscience : The Official Journal of the Society for Neuroscience, 29*(37), 11540-11549.

Zhang, M., Schwemmer, M. A., Ting, J. E., Majstorovic, C. E., Friedenberg, D. A., Bockbrader, M. A., et al. (2018). Extracting wavelet based neural features from human intracortical recordings for neuroprosthetics applications.*Bioelectronic Medicine, 4*(1), 11.